Bulletin of Volcanology (2024) 86:83
https://doi.org/10.1007/s00445-024-01773-1

RESEARCH ARTICLE

New evidence of syn-eruptive magma-carbonate interaction: the case study of the Pomici di Avellino eruption at Somma-Vesuvius (Italy)

Daniela Mele[1] · Marco Knuever[1] · Pierfrancesco Dellino[1] · Antonio Costa[2] · Annamaria Fornelli[1] · Silvia Massaro[1,2] · Roberto Sulpizio[1,2,3]

Received: 18 April 2024 / Accepted: 11 September 2024
© The Author(s) 2024

Abstract
Calcareous lithics are commonly found within the products of some explosive eruptions of Somma-Vesuvius. The pumice fragments from the final phase of the Plinian fallout event of the Pomici di Avellino eruption contain abundant calcareous xenoliths. Previous work on that eruption, including numerical simulations, suggested that the release of CO_2 from the entrapment of carbonates may have prolonged the magmatic phase of the eruption by maintaining sufficient driving pressure in the feeding dike. The texture and thermo-metamorphic reactions of carbonate xenolith-bearing pumice fragments of the Pomici di Avellino eruption are analyzed through petrography, scanning electron microscope images, energy dispersive spectrometer analyses, and micro-computed X-ray tomography to deduce the behavior of short-term carbonate-magma interaction and its contribution to the eruption dynamics. Results show that calcareous xenoliths experienced short-term magma-carbonate interaction, which took place in three steps: (i) entrainment, i.e., the mechanical process of carbonate xenoliths entrapment into a magma; (ii) decarbonation, related to high-temperature decomposition reaction of the xenoliths; and (iii) digestion or dissolution of the incorporated calcareous xenoliths into the melt with diffusion of Ca and Mg. The CO_2 released during the syn-eruptive decarbonation process thus provided extra volatiles to the rising magma, which may have maintained magma buoyancy longer than expected if only magmatic volatiles were involved in the eruption.

Keywords Pomici di Avellino eruption · Magma-carbonate interaction · Carbonate assimilation · Magma ascent · Explosive volcanism · Eruptive behavior

Introduction

The interaction of magma with country rocks, especially with carbonate-bearing rocks, is a process of paramount importance in driving and sustaining eruption dynamics. The thermo-metamorphic reaction undergone by carbonates may release volatiles (mainly CO_2) into the magmatic system (Blythe et al. 2015; Borisova and Bohrson 2023), which can increase magma ascent rate at hazardous volcanoes like Somma-Vesuvius (Italy), Merapi (Indonesia), Popocatépetl (Mexico), and Yellowstone (USA; Goff et al. 2001; Werner and Brantley 2003; Schaaf et al. 2005; Chadwick et al. 2007; Iacono-Marziano et al. 2009; Deegan et al. 2010, 2011; Dallai et al. 2011; Troll et al. 2012, 2013; Borisova et al. 2013; Jolis et al. 2015). Due to its very low solubility in magmas at shallow crustal depths (e.g., Lowenstern 2001), the release of CO_2 largely affects the magmatic evolution, magma ascent, and eruptive dynamics via processes like CO_2 flushing in both mafic and felsic magmas even when calcareous wall rocks are absent (Giuffrida et al. 2017; Caricchi et al. 2018, 2024; Pappalardo et al. 2023). However, to comprehensively describe the effect the release of CO_2 may have on eruption dynamics, it is indispensable to account for the CO_2 derived from the interaction of magma with carbonate-bearing wall rocks.

Long-term magma-carbonate interaction, which usually occurs around magma chambers or sills, is a largely studied process that may induce silica undersaturation in magmas (Iacono-Marziano et al. 2008; Mollo et al. 2010). These

Editorial responsibility: P.-S. Ross

✉ Daniela Mele
daniela.mele@uniba.it

[1] Dipartimento di Scienze della Terra e Geoambientali, Università degli Studi di Bari "Aldo Moro", Bari, Italy

[2] INGV, Bologna Section, Via D. Creti 12, Bologna, Italy

[3] IGAG-CNR, Via M. Bianco, Milan, Italy

Published online: 20 September 2024

long-term interactions are shown by the presence of skarn xenoliths (weakly-to-highly metamorphosed carbonate and calcium-silicate rocks), the isotope composition of magmatic minerals and contaminated melt, and the chemistry of gas released from fumaroles (Freda et al. 1997; Mason et al. 2017). In particular, long-term magma-carbonate interaction has been invoked for explaining magma genesis at Somma-Vesuvius (del Moro et al. 2001; Gilg et al. 2001; Fulignati et al. 2004; Iacono-Marziano et al. 2009; Dallai et al. 2011; Pichavant et al. 2014; Jolis et al. 2015).

In turn, short-term magma-carbonate interaction, which occurs as a syn-eruptive process within the volcanic feeding system, is less known. Experiments on magma-carbonate interaction (Deegan et al. 2010; Troll et al. 2012; Jolis et al. 2013; Blythe et al. 2015; Knuever et al. 2023) have shown that this interaction is a fast process (minutes to tens of minutes) suggesting that it can be effective during the rapid magma ascent of explosive eruptions. Syn-eruptive entrainment of carbonate wall rock has been identified as a process that affected the eruptive dynamics of several explosive eruptions at Colli Albani (e.g., Pozzolane Rosse eruption, Freda et al. 2011; Prata Porci and Albano maar eruptions, Cross et al. 2014; Sottili et al. 2009, 2010). Ca-carbonate xenoliths are also common in some of the explosive eruptions of Somma-Vesuvius (e.g., Fulignati et al. 2004), such as the Pomici di Avellino (Sulpizio et al. 2010), Pompeii (Jolis et al. 2015), Pollena (Sulpizio et al. 2005), and 1631 AD (Rosi et al. 1993) eruptions, but their short-term contribution to the eruption dynamics was only discussed for the Plinian Pomici di Base eruption (Pappalardo et al. 2018; Buono et al. 2020).

Therefore, in order to investigate the importance of the syn-eruptive processes of magma-carbonate interaction for several highly explosive eruptions at Somma-Vesuvius, this paper focuses on the Pomici di Avellino eruption (3.9 cal. ky BP, Sevink et al. 2011). The pumice fragments from the final phase of the Plinian fallout (EU3; Sulpizio et al. 2010; Hanson 2016) contain abundant Ca-carbonate xenoliths, entrapped from the Mesozoic carbonate sequence present in the subsurface of the volcano (e.g., Santacroce 1987). Xenoliths were most likely entrained due to the deepening of the fragmentation level over time (Sulpizio et al. 2010) and due to partial feeding dike wall collapses as a result of the beginning closure of the feeding dike heralding the progressive exhaustion of driving pressure (Costa et al. 2009; Massaro et al. 2018). Both Sulpizio et al. (2010) and Massaro et al. (2018) suggested that the release of CO_2 from the entrapment of carbonates may have prolonged the magmatic phase of the eruption by maintaining sufficient driving pressure in the feeding dike.

In the present work, in order to examine the behavior of short-term carbonate-magma interaction and its contribution to the eruption dynamics, the texture and thermo-metamorphic reactions of carbonate xenolith-bearing pumice fragments were analyzed through petrographic description, scanning electron microscope (SEM) images, and energy dispersive spectrometer (EDS) analyses. Micro-computed X-ray tomography (μ*X-CT*) highlighted the 3D morphology and internal structure of the carbonate-bearing pumice fragments. The collected data shed light on the syn-eruptive processes of magma-carbonate interaction at Somma-Vesuvius and discuss its contribution to eruption dynamics.

Brief overview of Pomici di Avellino eruption

The Pomici di Avellino eruption (PdA) is characterized by three main eruptive phases (opening, magmatic Plinian, and phreatomagmatic), which formed five eruptive units (EU1–EU5; Sulpizio et al. 2010). During the opening phase, characterized by two brief sustained columns (EU1a, b; heights of 13 and 21.5 km, respectively; Sulpizio et al. 2010), thin fall deposits and minor pyroclastic density currents were dispersed onto the volcano slopes. The Plinian magmatic phase emplaced widespread fall deposits, comprising white phonolitic (EU2) and grey tephriphonolitic (EU3) pumice fallouts. EU2 exhibits a reversely graded deposit, with eruption intensity increasing over time (Sulpizio et al. 2010). Maximum column height is estimated at ~23 km, with a mass discharge rate (MDR) of $\sim 5.7 \times 10^7$ kg/s (Sulpizio et al. 2010). The transition from EU2 to EU3 is marked by a layer of white–grey banded pumice clasts, indicating syn-eruptive mingling between magma sources. Column height reached ~31 km in EU3, corresponding to an MDR of $\sim 1.7 \times 10^8$ kg/s (Sulpizio et al. 2010), with a fall deposit volume ~1.0 km^3. One small pyroclastic density current deposit was recognized due to partial column collapse (Sulpizio et al. 2010).

Following a brief eruptive pause after EU3, marked by a thin ash layer, activity resumed with the establishment of a short-lived sustained column depositing EU4 fall deposits (Sulpizio et al. 2010). The PdA eruption ended with a phreatomagmatic phase (EU5, Sulpizio et al. 2010), characterized by the emplacement of major PDCs and minor fall deposits.

Accessory lithics, represented by lavas, tuffs, limestones, marbles, cumulate rocks, skarns, and syenites, changed in amount and type during the PdA eruption (Sulpizio et al. 2010). Regarding the Plinian phase, accessory lithics are mainly lavas in EU2 deposits and limestones and marbles in EU3 deposits (Sulpizio et al. 2010). Carbonate xenoliths (CXs) within pumice clasts occur in the upper part of the EU3 deposit and have been quantified to 3–4 wt.% by Hanson (2016).

Materials and methods

We sampled pumice fragments at five different stratigraphic heights of the EU3 fallout deposit (Fig. 1a), in a location at about 4 km north of the Vesuvius crater (denoted as Site B in Sulpizio et al. 2010). Pumices were randomly selected at each stratigraphic height. CXs, which are well visible and enclosed in pumice fragments at the top of the deposit (see number 5 in Fig. 1a), are covered by a white patina (Fig. 2). Hereby, we define patina as a poorly indurated external shell, which has different texture with respect the inner part of the clast.

Pumice fragments from the base and top of EU2 and EU3 fallout deposits (samples 1 and 2 of the EU2 deposit, and samples 1 and 5 of the EU3 deposit; Fig. 1a) were analyzed to reconstruct their vesicle size distribution. For the EU3 pumice fragments, the weight percentage of CXs within pumices was assessed, and the textures and reaction products of CXs with magma were investigated.

Macroscopic analysis

Pumice fragments from the five samples of the EU3 fallout deposit (Fig. 1a) were gently crushed in order to collect and weigh the CXs. The size of the CXs was measured using a caliper (on extracted fragments) or by *μX-CT* analysis ("X-Ray micro-tomography (μX-CT) analysis" Section).

Petrography

Textural-petrographic analysis was performed, using a polarized optical microscope, on thin sections obtained from six CX-bearing pumices of the number 5 sample at the top of EU3 (Fig. 1a).

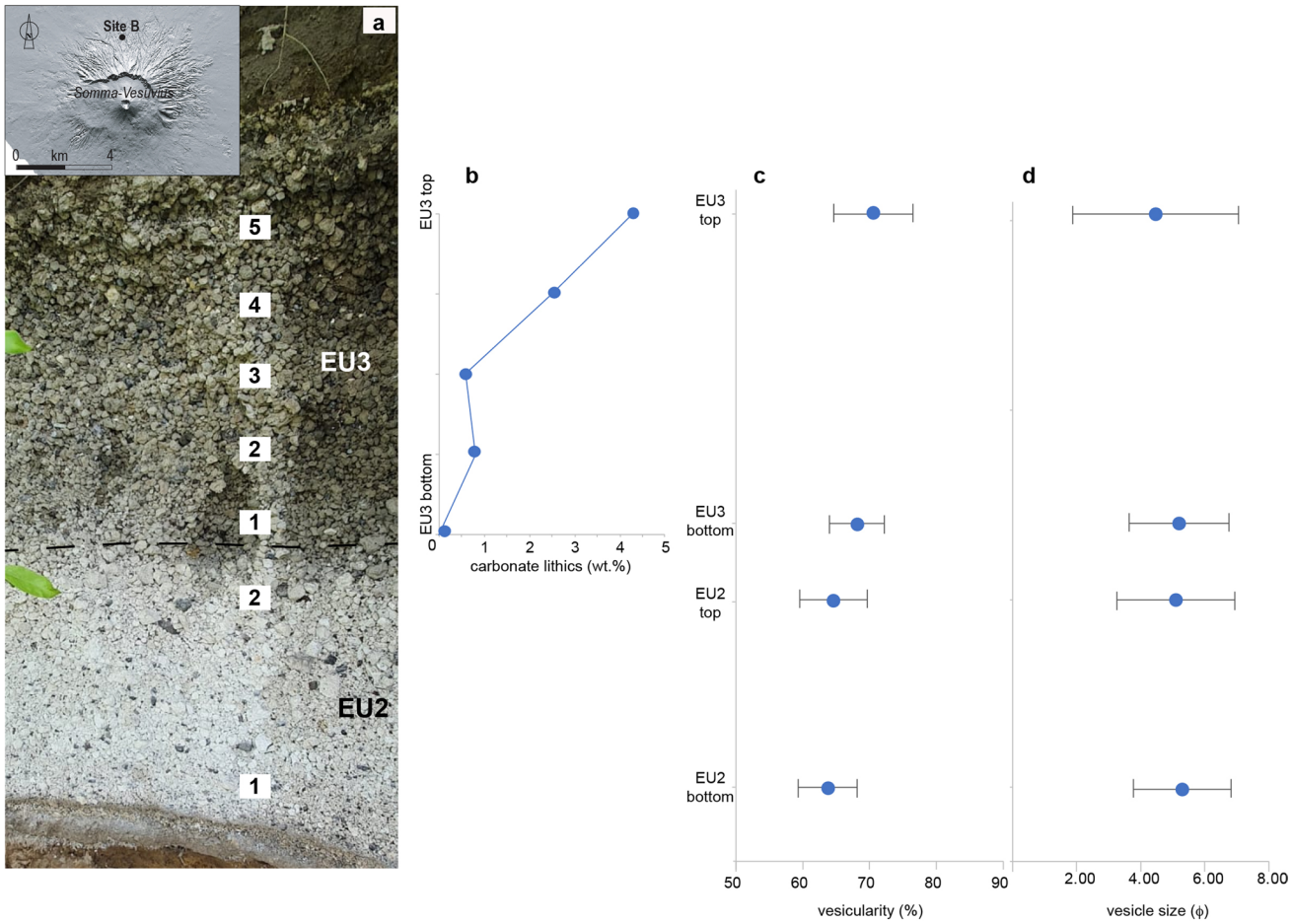

Fig. 1 **a** Field picture of the PdA fall deposits (EU2 and EU3). The numbers on the picture are the collected samples (two for EU2 and five for EU3). In the insert, outcrop location of the collected samples (denoted as Site B in Sulpizio et al. 2010). **b** Vertical variation of the weight percentage of carbonate xenoliths inside juvenile fragments of the EU3 unit. **c** and **d** Vertical variation of vesicularity (%) and vesicle size of juvenile fragments of the four samples analyzed by μX-CT scanner

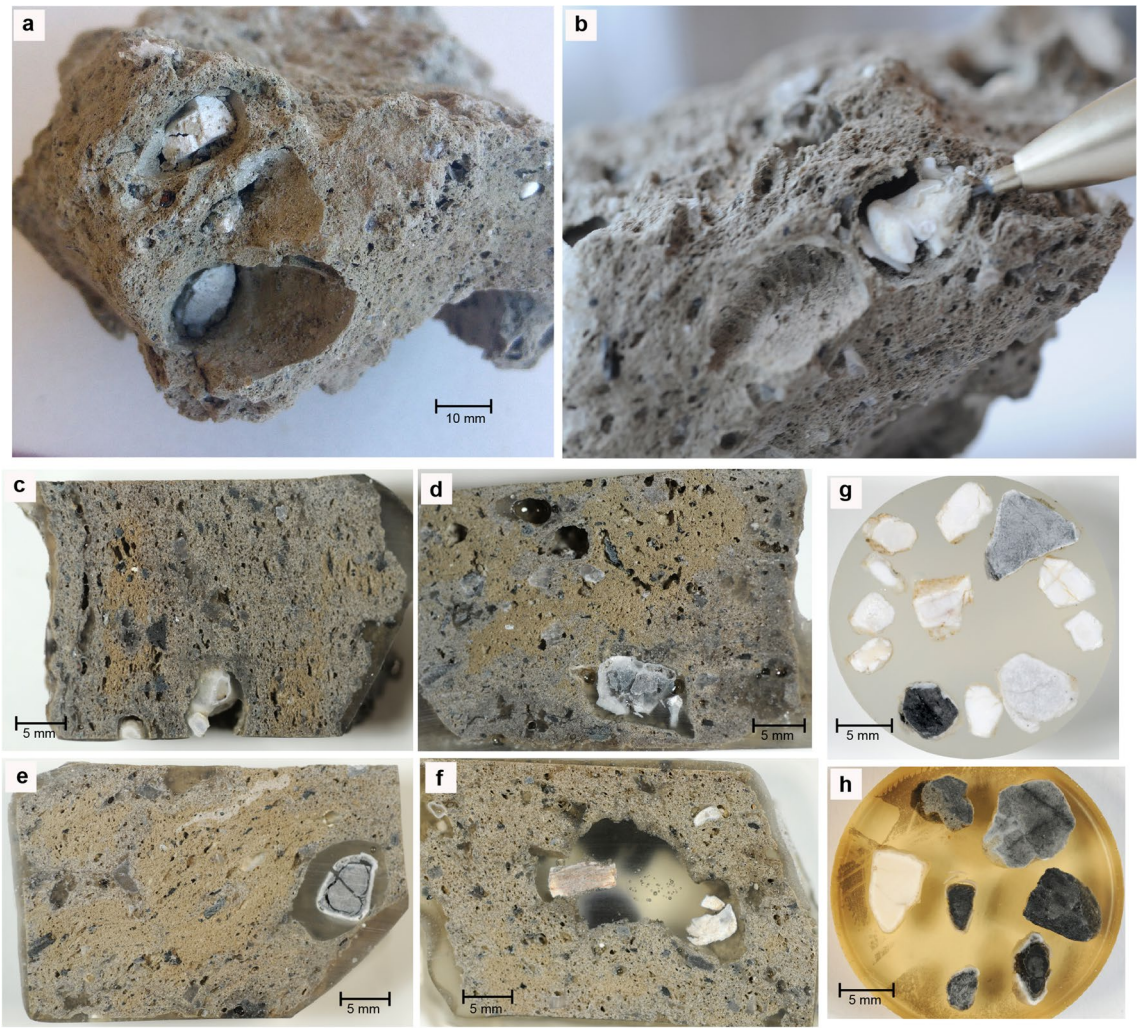

Fig. 2 Pictures of some carbonate xenoliths inside juvenile fragments of EU3 units. **a** and **b** Within intact juvenile fragments. **c**, **d**, **e**, and **f** Within cut juvenile fragments embedded in epoxy resin. **g** and **h** Selected carbonate xenoliths embedded in epoxy resin

Scanning electron microscopy and energy dispersive spectrometry (SEM + EDS)

Ten CX-bearing pumices and 12 CX fragments of the sample at the top of the EU3 unit (sample number 5; Fig. 1a) were embedded in epoxy resin and polished for EDS analysis (Fig. 2c–h). The images were acquired using an SEM (LEO EVO-50XVP of Zeiss Cambridge), while EDS analysis was carried out through the coupled Oxford-Link Ge ISIS equipped with a Super Atmosphere Thin Window©. The SEM analyses were carried out using backscattered electrons (BSE) with a 15 kV accelerating potential, 500 pA probe current, ~ 25,000 output counts per second (cps) as an average count rate on the whole spectrum, counting time of 50 s, and 8.5 mm working distance. For elemental composition analysis, X-ray intensities obtained by the EDS spectrometer were converted to wt.% oxides by the ZAF4/FLS quantitative analysis software of Oxford-Link Analytical. Given the composition of the analyzed phases, the 1σ precision corresponds to the following values: $SiO_2 = 0.10–0.20$ wt%, $TiO_2 = 0.08–0.10$ wt%, $Al_2O_3 = 0.08–0.13$ wt%, $FeO = 0.05–0.15$ wt%, $MnO = 0.04–0.6$ wt%, $MgO = 0.08–0.13$ wt%, $CaO = 0.04–0.14$ wt%, $Na_2O = 0.04–0.06$ wt%, and $K_2O = 0.04–0.12$ wt%. The accuracy of the analytical data was also checked using several standard minerals manufactured by Micro-Analysis Consultants Ltd (Caggiani et al. 2015). To compare the chemical data obtained on the pumices and CXs, the oxides were recalculated to 100% excluding the volatile component.

X-Ray micro-tomography (μX-CT) analysis

We selected two sets of CX-bearing pumice for μX-CT analysis. The first set was made up of pumice fragments of 16–22 mm size, sampled at the bottom and the top, respectively, of both the EU2 and the EU3 deposit (sample

numbers 1 and 2 of EU2 and sample numbers 1 and 5; Fig. 1a) in order to obtain their vesicularity and vesicle size distribution (VSD). We have taken seven pumices for each sample, for a total number of scanned pumices of 28. The second set was composed of eight CXs, extracted from pumices of sample number five of the EU3 deposit (Fig. 1a), for observing their 3D internal structures and textures.

We used a Bruker Skyscan 1172 high-resolution μX-CT scanner. The system is equipped with a polychromatic micro-focus X-ray tube. The parameters used to acquire μX-CT data are shown in Table 1. For the vesicularity and VSD, due to the presence of centimeter-sized vesicles, a multi-scale approach based on the pore number was applied to integrate different pore scale data (dos Reis et al. 2017; Nagata et al. 2023). We scanned, therefore, each pumice two times using two distinct pixel sizes, 2.17 μm and 21.7 μm (Table 1), obtaining two datasets of projection images.

Bruker's NRecon software was used to reconstruct μX-CT projection images into two-dimensional cross-sections (slices) by applying the Feldkamp algorithm (Feldkamp et al. 1984). Cross-section parameters are shown in Table 1. μX-CT datasets were analyzed and visualized using Bruker's CTAn and CTvox software. The vesicularity and VSD were obtained by selecting for each scanned pumice a volume of interest (VOI) of 160 mm^3 and 4000 mm^3 for the datasets of 2.17 μm and 21.7 μm, respectively. To extract vesicles from matrix glass and crystals, the raw images were segmented using the Otsu algorithm's automatic thresholding (Otsu 1979). The vesicularity was obtained as the percentage of the vesicle volume inside the VOI. The VSD was obtained using a sphere-fitting algorithm, which is based on two steps: "skeletonization" to identify the medial axis of all structures and sphere-fitting to measure the local thickness of all voxels lying along the medial axis (Remy and Thiel 2002). Later, to integrate the results obtained from measurements performed at two different spatial resolutions, a multiscale model proposed by dos Reis et al. (2017) was applied for both vesicularity and VSD. The average and standard deviation of the vesicularity were determined from the seven values of pumice fragments of each sample. The integrated VSD of each pumice was, instead, converted in φ unit using 0.25 ϕ intervals ($\phi = -\log_2(d)$, where d is the vesicle size in millimeters). The average volume percentage of each vesicle size fraction was calculated from the values of the seven pumice fragments of each sample. Finally, the median vesicle size and the standard deviation parameters (Inman 1952) of the average VSD of each sample were calculated using a Fortran code, available in the PYFLOW package (Dioguardi and Dellino 2014).

Regarding CXs, we scanned each xenolith using a pixel size of 2.44 μm (Table 1) to observe qualitatively their 3D internal structures and textures.

Results

Macroscopic analysis

The weight percent of CXs inside juvenile fragments increases, from bottom to top of the EU3 unit (site B, Fig. 1a), from 0.6 to 4.3 wt.% (Fig. 1b).

From a macroscopic observation of CXs, it appears that they can be split into two main categories, based on internal color, i.e., (dark-)grey and white CX fragments (Figs. 2, 3, and 4), which occur approximatively with the same abundance. All CXs show a white patina. The patina has different compactness. Some (dark-)grey CXs have a millimeter-thick smooth and indurated external patina (Fig. 4a and g). Other CXs exhibit unconsolidated patina (Figs. 3a, d, and g and 4d). The patina thickness ranges between 0.12 and 0.8 mm. Some of the white CXs show an inner corona more homogeneous with respect to the core, in addition to the patina (Fig. 3a, d). Hereby, we define the corona as a whitish area, texturally different from the inner part of CX (Fig. 3a, d). The corona thickness ranges between 0.1 and 0.7 mm.

Table 1 Scan parameters of the μX-CT scanner. I_a and I_b sample sets are used to determine the vesicle size distribution using two different pixel sizes. II sample set is used only for the carbonate xenoliths

		I_a sample set: pumices	I_b sample set: pumices	II sample set: xenoliths
X-CT scanner parameters	Pixel size (μm)	2.17	21.7	2.44
	X-ray voltage (kV)	100	71	100
	X-ray current (μA)	100	139	100
	Rotation step (degrees)	0.22	0.36	0.30
	Filter	Al + Cu	Al + Cu	Al + Cu
	Frame averaging	4	5	5
Reconstruction parameters	Smoothing	7	2	6
	Ring artifact correction	14	5	9
	Beam hardening correction	71	66	61

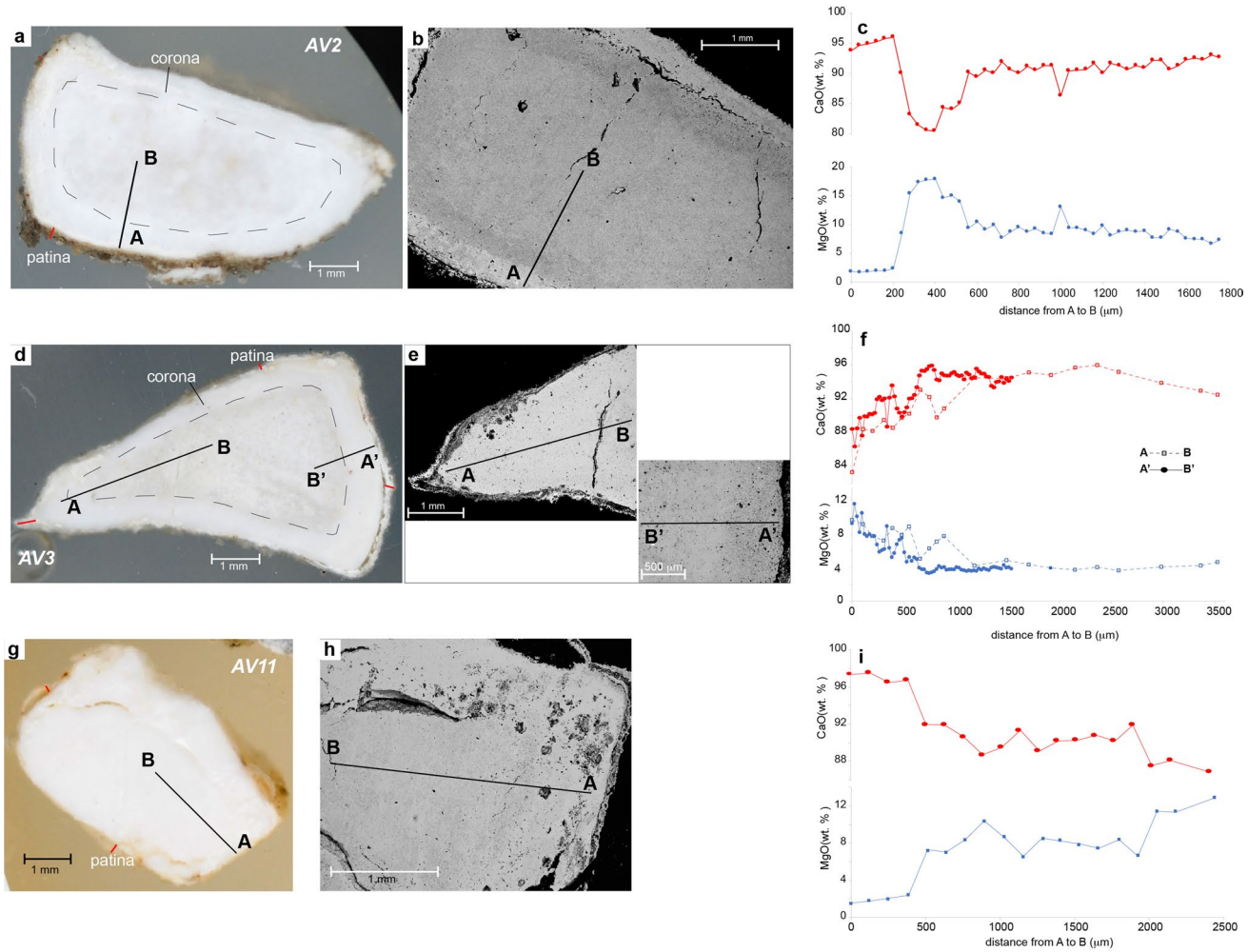

Fig. 3 Representative pictures of three cut white (**a**, **d**, **g**) carbonate xenoliths and their BSE images (**b**, **e**, **h**). In Tables 2 and 3, their chemical composition is reported. The diagrams (**c**, **f**, **i**) are the EDS analyses of traverses from the core (B) to the external border (A) of carbonate xenoliths. The blue and red lines represent MgO and CaO percentages (wt.%), respectively. The dashed line on the white xenoliths (**a**, **d**) shows the corona edge. The red lines on the three fragments show the patina thickness

The size range of the analyzed CXs (55 fragments) is between 0.1 and 1.5 cm.

Petrographic analysis

The analyzed CXs inside juvenile fragments (pumices) are limestone fragments. They show an amorphous rim without birefringence, representing the external patina. The latter is surrounded by acicular small calcite crystals (Fig. 5). The limestone fragments in the inner portions record the original texture of impure calcareous rocks (presence of Fe-hydroxides and clay minerals; Fig. 5). The partial dissolution of limestone fragments in the magma is evidenced by numerous and large voids in the amorphous and crystalline portions. In some cases, the CXs consist only of the amorphous carbonates, without the crystalline portions (Fig. 5c).

SEM + EDS analysis

The BSE images show an internal homogeneous texture of the CXs, with few pores that increase in abundance moving towards the rim of the clast (Figs. 3b, e, and h and 4b, e, and h). Fractures are also observed in many samples, as observed also by petrographic analysis (Figs. 3b, e, and h and 5). A dendritic texture is present inside the large pores (Figs. 3h and 4h).

The results of the EDS analysis of cores of the (dark-) grey CXs show that their chemical composition almost exclusively consists of CaO (96–99 wt.%; Table 2) with a low percentage (< 2 wt.%) of MgO and SiO_2. Al_2O_3, SrO, F, and Cl are present with a combined percentage < 0.55 wt.%. The white CX cores have a higher percentage of MgO than the (dark-)grey CXs (3.6–11.9 wt.%; Table 2),

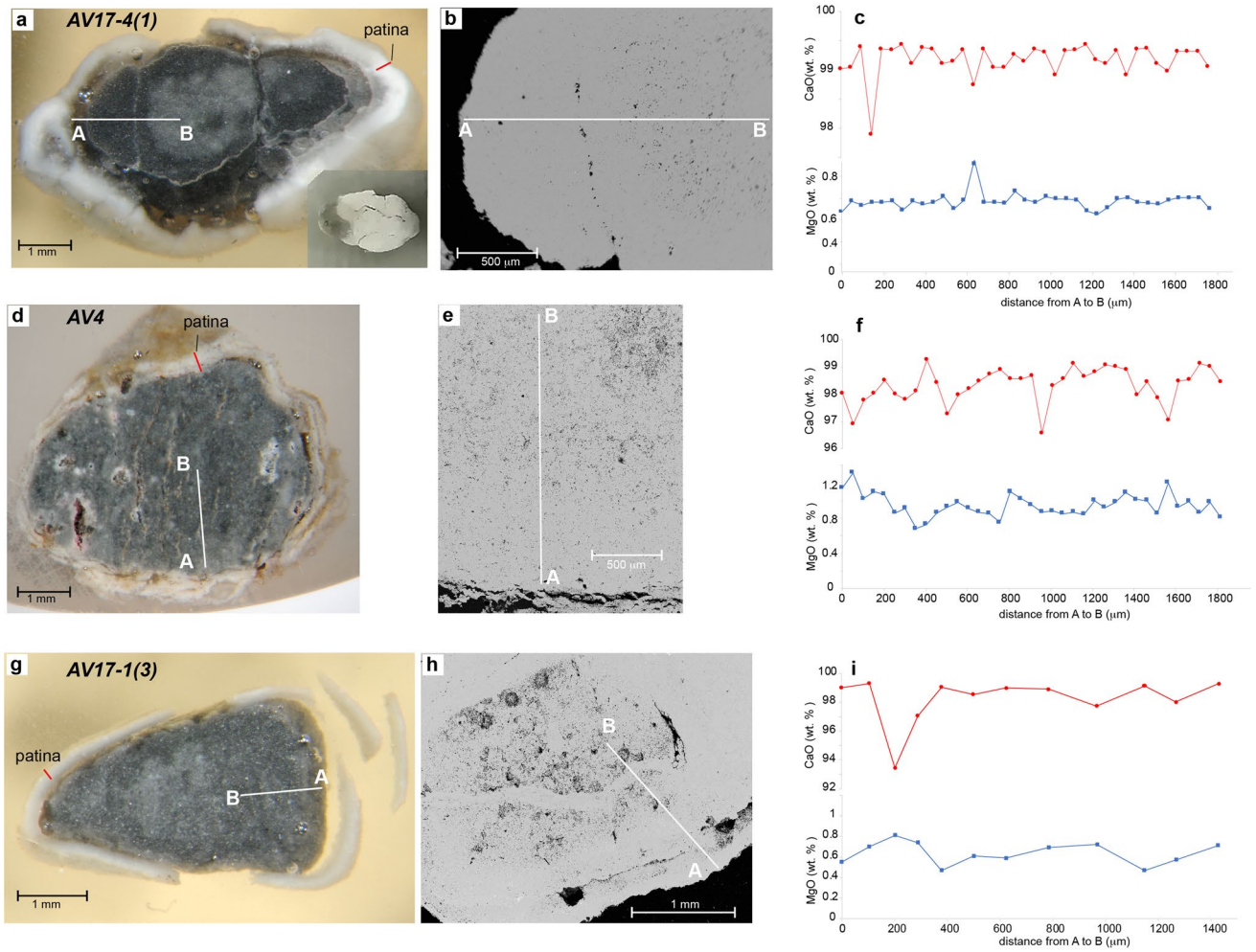

Fig. 4 Representative pictures of three cut (dark-)grey (**a**, **d**, **g**) carbonate xenoliths and their BSE images (**b**, **e**, **h**). In Tables 2 and 3, their chemical composition is reported. The diagrams (**c**, **f**, **i**) are the EDS analyses of traverses from the core (B) to the external border (A) of carbonate xenoliths. The blue and red lines represent MgO and CaO percentages (wt.%), respectively. The red lines on the three fragments show the patina thickness

while CaO ranges between 92 and 96 wt.%. SiO_2, Al_2O_3, F, and Cl are present with a total percentage < 1.5 wt.%.

The chemical data of transects (i.e., from the core to the rim of the CXs, excluding the patina) of the white CXs show a variation of CaO and MgO content (Fig. 3). Where the corona is clearly visible, it is observed an increase in the MgO within the corona, while simultaneously the CaO content decreases (Fig. 3d–f and Table 3). In other cases, the corona shows two different parts, which appear at different grey scales under BSE images (Fig. 3a, b). In this case, the inner corona is Mg-rich and Ca-poor, while the abundance is the reverse in the outer part of the corona (Fig. 3c). In a third case, where the corona is not visible, as shown in Fig. 3g–i, a continuous increase of CaO and decrease of MgO can be observed. The CaO and MgO variation has not been recorded in the (dark-)grey CXs (Fig. 4 and Table 3).

The patinas that showed an amorphous rim in the petrographic analysis show a complex texture in the BSE images (Figs. 5 and 6). Some, mainly from (dark-)grey CXs, show bands parallel to the CX border, with a more porous texture than the CX core (Fig. 6a). For the white and few (dark-)grey CXs, the patinas show areas with both cauliflower and highly porous dendritic texture, alternating with more dense texture (Fig. 6b). Areas with different BSE brightness are visible (Figs. 6 and 7), with the bright-grey areas being almost exclusively composed by CaO (91–98 wt.%) with a low concentration of Na_2O, MgO, Al_2O_3, SiO_2, and SrO (Fig. 6 and Table 4) and the darker grey areas (amorphous appearance) that are bordered by the Ca-rich zone, being characterized by a lower content of CaO (Figs. 6 and 7; Tables 4 and 5). In general, the different grey tones are related to their chemical compositions.

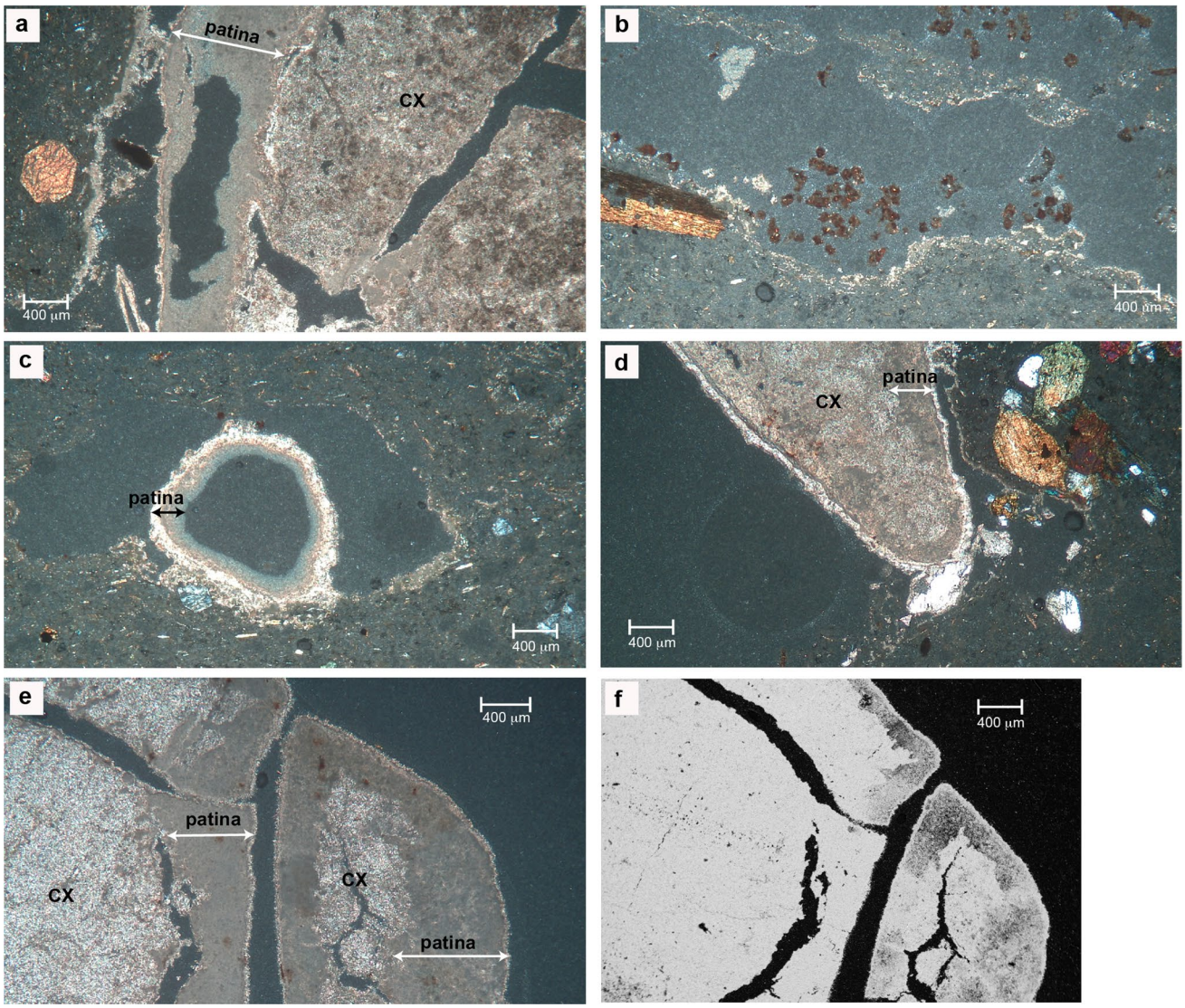

Fig. 5 Photomicrographs of (dark-)grey xenoliths inside juvenile fragments (**a**, **b**, **c**, **d**, and **e**). **f** BSE image of the xenolith (**e**)

A similar trend was observed in the areas between vesicular glass in contact with the CXs (Fig. 7).

At the outer edge of the patina, the Ca-rich zone shows acicular crystals, which sometimes result in a rosette-shaped organization (Galan et al. 2015; Figs. 6c–f and 7c). When the external patina of the CXs is in contact with the vesicular glass, melt enclaves are visible in the patina (Figs. 6d and 7). The glass inside these enclaves and the vesicular glass close to the patina have higher CaO contents and a more variable content of the other elements (Fig. 7 and Table 5) when compared to the glass portion more distant to the CXs, or in juvenile fragments (pumices) without CXs (Table 5). The CaO-rich zone varies in thickness but is always in the range of a few micrometers (Fig. 7).

X-ray microtomography analysis

The µX-CT analysis of pumice vesicularity shows a continuous increase in the average vesicularity from EU2 bottom to EU3 top (Fig. 1c). The standard deviation values increase within each eruptive unit (EU2 and EU3) going from the bottom to the top, with the juvenile fragments of the EU3 top sample having the maximum value (Fig. 1c) in agreement with Sulpizio et al. (2010). The vesicle size distributions of pumice fragments from the bottom and the top of the EU2 and EU3 beds show a faint poly-modality (Fig. 8). The smaller vesicle subpopulations are common in all samples (size greater than 5 ϕ) and represent the largest portion of the vesicle population (Fig. 8). The vesicle-size distribution is quite homogenous through EU2

Table 2 The average and standard deviation of major element composition of the core in white and (dark-)grey carbonate xenoliths, obtained by EDS spectrometer and given in wt.%

		Na2O	MgO	Al2O3	SiO2	SO3	K2O	CaO	TiO2	MnO	FeO	SrO	F	Cl
Black-grey	AV17-1(2)	-	1.26 ± 0.26	0.27 ± 0.19	1.11 ± 0.78	-	-	97.36 ± 1.22	-	-	-	-	-	-
	AV17-4(1)	-	0.66 ± 0.04	-	-	0.07 ± 0.16	-	99.20 ± 0.17	-	-	-	-	0.07 ± 0.16	-
	AV17-1(3)	-	0.59 ± 0.11	0.19 ± 0.00	0.76 ± 0.00	0.04 ± 0.00	-	98.24 ± 0.00	-	-	-	-	-	-
	AV4	-	1.36 ± 0.50	0.17 ± 0.24	1.14 ± 0.83	0.14 ± 0.83	-	96.16 ± 1.85	-	-	-	0.54 ± 0.19	0.51 ± 0.11	-
	AV6	-	0.96 ± 0.14	-	0.38 ± 0.33	0.06 ± 0.15	-	98.45 ± 0.74	-	-	-	-	0.15 ± 0.36	-
White	AV2	0.03 ± 0.08	7.78 ± 0.86	0.03 ± 0.08	-	0.04 ± 0.11	-	92.09 ± 0.84	-	-	-	-	-	0.03 ± 0.06
	AV3	-	3.94 ± 0.16	0.32 ± 0.16	1.51 ± 0.31	0.03 ± 0.09	-	94.20 ± 0.48	-	-	-	-	-	-
	AV5	0.07 ± 0.15	4.38 ± 0.15	0.42 ± 0.06	1.19 ± 0.38	0.44 ± 0.04	-	92.76 ± 0.52	-	-	-	-	0.67 ± 0.18	0.07 ± 0.08
	AV7	0.06 ± 0.12	3.59 ± 0.89	-	0.10 ± 0.20	0.21 ± 0.15	-	95.78 ± 0.72	-	-	-	-	0.24 ± 0.48	0.03 ± 0.06
	AV8	-	3.73 ± 0.51	0.05 ± 0.11	-	-	-	96.22 ± 0.61	-	-	-	-	-	-
	AV9	-	3.94 ± 0.88	0.04 ± 0.09	-	0.44 ± 0.09	-	95.30 ± 0.08	-	-	-	-	0.25 ± 0.36	0.02 ± 0.04
	AV11	-	11.87 ± 0.87	0.11 ± 0.19	-	-	-	87.46 ± 0.64	-	-	-	-	0.28 ± 0.49	0.25 ± 0.04

to EU3 bottom (Fig. 8e). The EU3 top shows a decrease in the finer vesicle distribution and an increase in 3–5 ϕ population (Fig. 8e–f). The maximum dimension among analyzed vesicles is about 2 mm for the juvenile fragments of EU2 (bottom and top), and EU3 bottom and 8 mm for EU3 top (− 3 ϕ; Fig. 8). The juvenile fragments of the EU3 top layer have a broader vesicle size distribution with respect to EU2 (bottom and top) and EU3 bottom pumice clasts (Figs. 1d and 8).

The CXs inside the scanned pumices are quickly identified both due to the different grey color scale and due to the presence of a patina (Figs. 9 and 10).

Unlike other types of lithics and (loose) crystals, the *μX-CT* images show a wide empty space between the glass and CXs. Some vesicles exhibit pipe-like structures (Fig. 10a). The patina surface is rough (Fig. 10); it completely envelops the CXs, smoothing its shape, with a thickness, measured both by *μX-CT* images and thin sections, ranging between 50 and 350 μm. The corona of white CXs was not recognized by μX-CT analysis (AV3 CX, Figs. 3d and 10).

Material with a lower attenuation coefficient value than the bulk CX is scattered both on the surface and inside the patina of all analyzed CXs (red areas in Fig. 10). It can be correlated with different areas that have a lower percentage of CaO and a higher percentage of MgO, Al_2O_3, SiO_2, and FeO (see the "Heating of clasts and volatile release" section).

Some small CXs with grain sizes less than 2 mm show ample space between the patina and inner part of the CX and abundant fractures in the core (Fig. 9c).

Discussion

Following the nomenclature proposed by Knuever et al. (2022), the carbonate wall rock-magma interaction consists of a three-step process: (i) entrainment, only due to the mechanical process of CX entrainment into a magmatic body; (ii) decarbonation, related to the thermal or contact metamorphic effect of heating of CXs; and (iii) digestion or dissolution due to surface reaction and/or the diffusive transport of Ca (± Mg) from the incorporated CXs into the melt. The textural and geochemical analysis of this study suggests that the limestone CXs enclosed in pumice fragments during the EU3 phase of the PdA eruption underwent a non-complete assimilation process, mostly reduced to decarbonation and only partial dissolution. In the following, we will discuss the three different steps, providing inferences on how they have influenced the eruptive style and duration of the eruption.

Table 3 The average and standard deviation of major element composition along the traverses of white and (dark-)grey carbonate xenoliths from the core to the external border of clasts, excluding the patina, obtained by EDS spectrometer and given in wt.%. The maximum and the minimum value of chemical elements found along the traverses are written in parentheses

		Na2O	MgO	Al2O3	SiO2	SO3	K2O	CaO	TiO2	MnO	FeO	SrO	F	Cl
Black-grey	AV17-1(2)	-	1.16 ± 0.20 (1.54/0.92)	0.12 ± 0.17 (0.41/0.00)	0.69 ± 0.61 (1.84/0.00)	0.03 ± 0.11 (0.35/0.00)	-	98.00 ± 0.92 (99.8/96.21)	-	-	-	-	-	-
	AV17-4(1)	0.01 ± 0.04 (0.22/0.00)	0.65 ± 0.08 (1.02/0.53)	0.01 ± 0.03 (0.19/0.00)	0.03 ± 0.07 (0.27/0.00)	0.04 ± 0.10 (0.35/0.00)	0.01 ± 0.05 (0.29/0.00)	99.18 ± 0.28 (99.44/97.89)	-	-	-	-	0.09 ± 0.15 (0.42/0.00)	0.00 ± 0.02 (0.10/0.00)
	AV17-1(3)	-	0.64 ± 0.11 (0.81/0.47)	0.20 ± 0.27 (0.82/0.00)	0.83 ± 1.01 (3.35/0.00)	-	-	98.13 ± 1.72 (99.30/93.43)	-	-	-	-	0.19 ± 0.49 (1.59/0.00)	0.01 ± 0.03 (0.10/0.00)
	AV4	-	1.29 ± 0.37 (1.71/1.00)	0.26 ± 0.23 (0.43/0.00)	1.21 ± 0.60 (1.72/0.55)	0.09 ± 0.16 (0.27/0.00)	-	96.26 ± 1.23 (97.47/94.85)	-	-	-	0.36 ± 0.34 (0.67/0.00)	0.54 ± 0.10 (0.61/0.43)	-
	AV6	0.08 ± 0.16 (0.77/0.00)	0.95 ± 0.13 (1.31/0.68)	0.04 ± 0.09 (0.32/0.00)	0.35 ± 0.27 (1.13/0.00)	0.12 ± 0.16 (0.40/0.00)	-	98.34 ± 0.64 (99.27/96.58)	-	-	-	-	0.09 ± 0.22 (0.89/0.00)	0.04 ± 0.09 (0.44/0.00)
White	AV2	0.00 ± 0.03 (0.22/0.00)	9.02 ± 4.00 (17.99/1.79)	0.04 ± 0.09 (0.35/0.00)	0.21 ± 0.30 (1.33/0.00)	0.15 ± 0.17 (0.48/0.00)	-	90.25 ± 3.78 (96.08/80.49)	-	-	-	-	0.25 ± 0.62 (2.32/0.00)	0.08 ± 0.10 (0.32/0.00)
	AV3	-	5.17 ± 2.01 (11.53/3.33)	0.27 ± 0.15 (0.53/0.00)	1.27 ± 0.51 (3.07/0.53)	0.22 ± 0.28 (0.90/0.00)	-	93.04 ± 2.34 (95.91/86.36)	-	-	-	-	-	0.04 ± 0.07 (0.27/0.00)
	AV5	0.01 ± 0.07 (0.34/0.00)	4.50 ± 0.23 (4.93/3.99)	0.29 ± 0.15 (0.52/0.00)	0.71 ± 0.47 (1.79/0.00)	0.40 ± 0.05 (0.48/0.26)	-	93.28 ± 0.58 (94.24/92.03)	-	-	-	-	0.75 ± 0.29 (1.65/0.45)	0.05 ± 0.05 (0.19/0.00)
	AV7	0.02 ± 0.06 (0.24/0.00)	4.75 ± 1.55 (8.24/2.81)	0.02 ± 0.06 (0.21/0.00)	0.07 ± 0.15 (0.48/0.00)	0.26 ± 0.17 (0.53/0.00)	-	94.66 ± 1.56 (96.69/91.11)	-	-	-	-	0.16 ± 0.32 (0.95/0.00)	0.06 ± 0.07 (0.19/0.00)
	AV8	0.03 ± 0.14 (0.57/0.00)	6.94 ± 3.41 (13.94/3.40)	0.06 ± 0.10 (0.25/0.00)	0.15 ± 0.22 (0.61/0.00)	0.18 ± 0.21 (0.55/0.00)	-	92.43 ± 4.00 (96.60/85.54)	-	-	-	-	0.14 ± 0.43 (1.77/0.00)	0.07 ± 0.12 (0.39/0.00)
	AV9	0.01 ± 0.05 (0.20/0.00)	3.47 ± 0.81 (5.26/2.00)	0.05 ± 0.10 (0.31/0.00)	0.17 ± 0.20 (0.48/0.00)	0.50 ± 0.13 (0.69/0.32)	-	95.46 ± 1.00 (97.65/94.06)	-	-	-	-	0.35 ± 0.40 (1.28/0.00)	0.01 ± 0.02 (0.09/0.00)
	AV11	-	7.31 ± 3.32 (12.90/1.54)	0.06 ± 0.13 (0.33/0.00)	0.44 ± 0.35 (1.04/0.00)	0.14 ± 0.22 (0.58/0.00)	-	91.41 ± 3.31 (97.51/86.82)	-	-	-	-	0.56 ± 0.57 (1.37/0.00)	0.08 ± 0.10 (0.28/0.00)

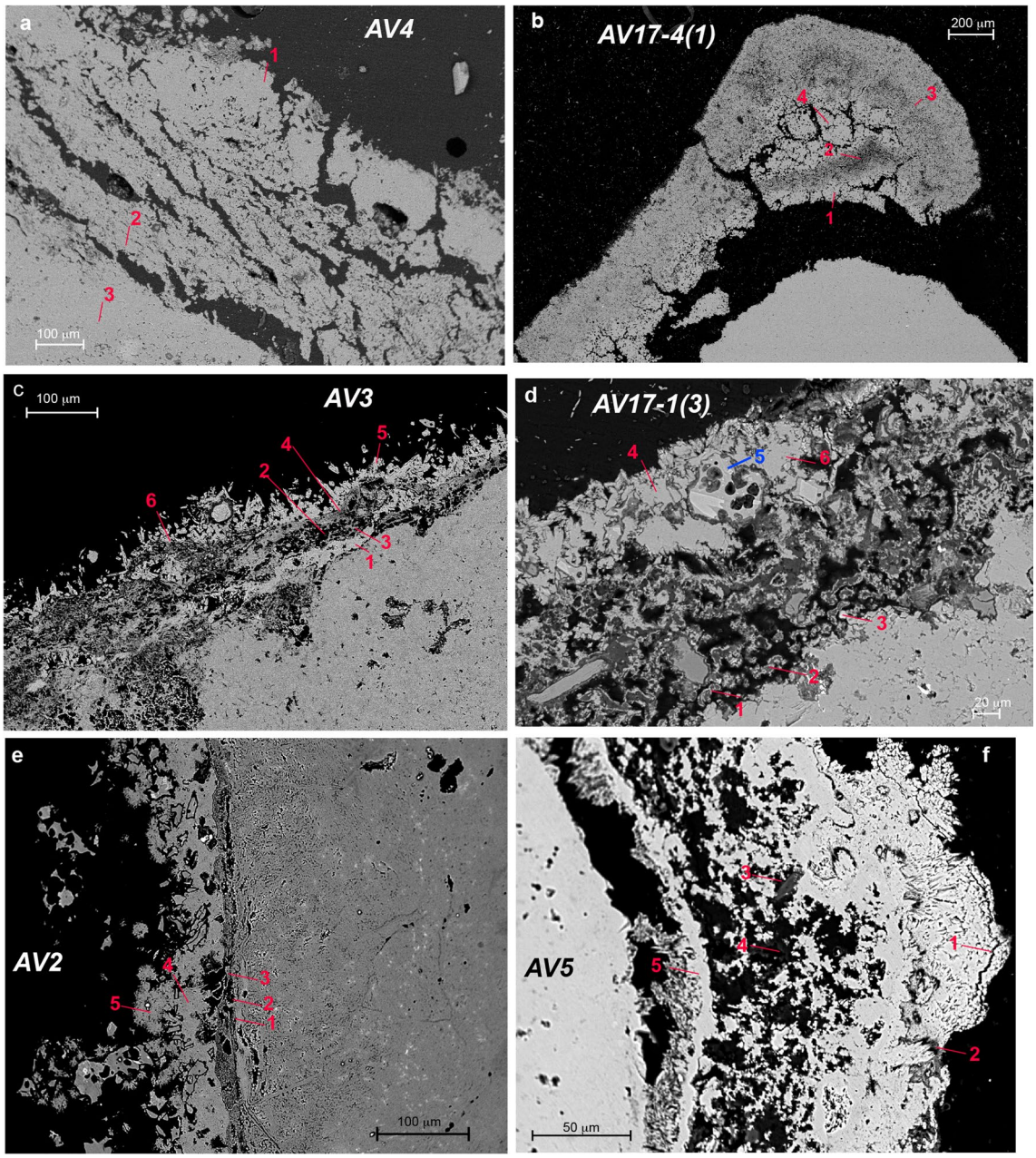

Fig. 6 Representative BSE images of the patinas of some CXs, with their chemical composition reported in Table 3. The red numbers represent the points whose chemical compositions are shown in Table 4. The blue line and number represent the PdA glass. **a** Patina of (dark-)grey CX with bands parallel to the CX border; **b** (dark-)grey CX with cauliflower patina; **c**, **d**, **e**, and **f** patinas with highly porous dendritic texture

Entrainment of clasts within magma

Since the carbonate rocks are included as xenoliths within the juvenile pumice, they must have been eroded from the feeding dike walls and entrained into the magma below (before) the magma fragmentation level, favoring fast decarbonation thanks to direct contact with hot magma. Since the pumices containing carbonate clasts are found mainly at the top of the EU3-Plinian fallout deposit, it is likely that their entrainment has been favored by the progressive closure of the feeding dike towards the end of the eruption. If the magmatic overpressure then drops below the lithostatic one, the feeding dike will respond elastically (i.e., a progressive decrease of the feeding dike width in response to changed pressure conditions). Hence, the feeding dike walls become highly unstable and might partially collapse, entraining more carbonate wall rocks from the feeding dike walls into the magma (Costa et al. 2009; Massaro et al. 2018).

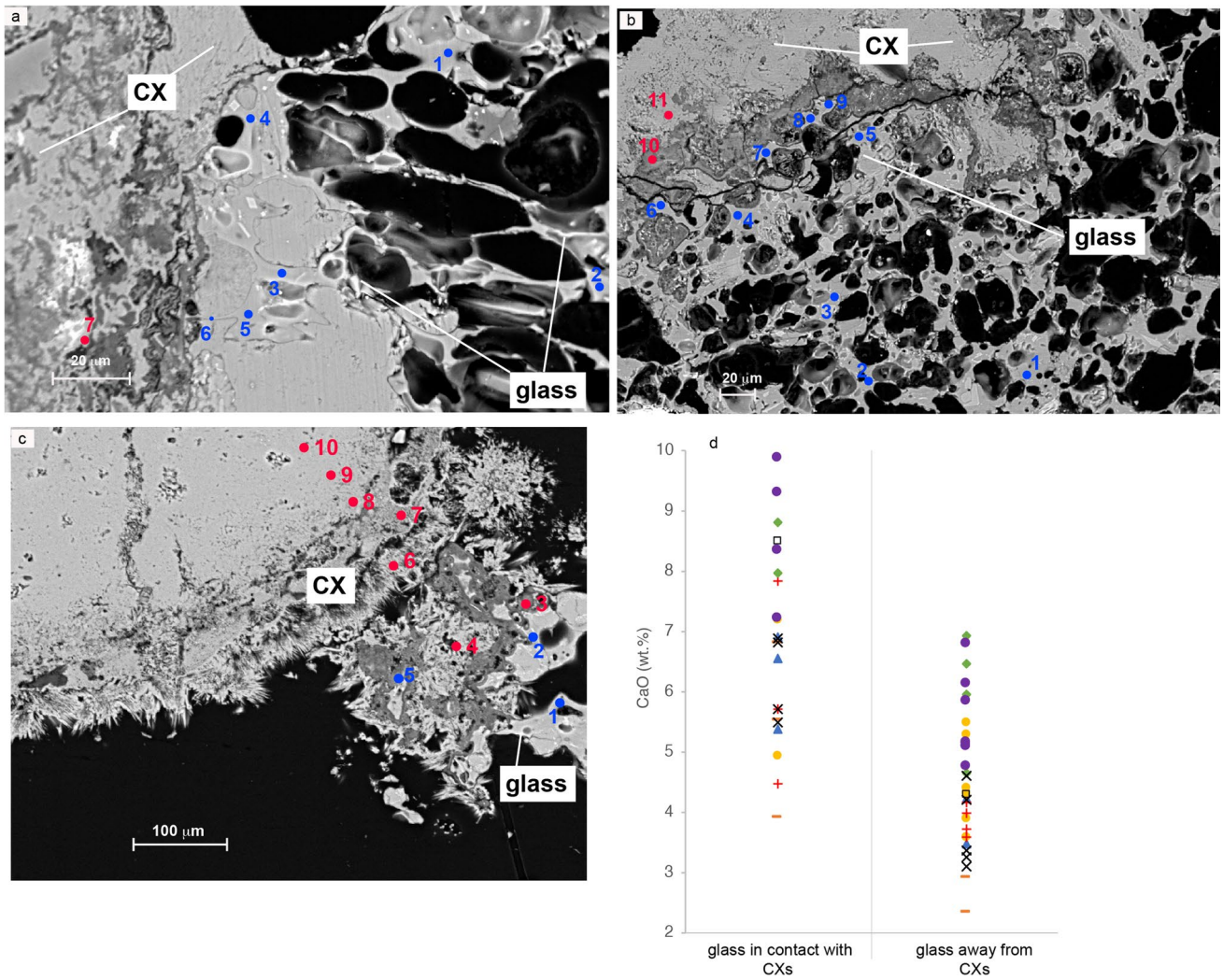

Fig. 7 Representative BSE images (**a**, **b**, **c**) of the external patina of CXs in contact with the vesicular glass of the pumices. The numbers represent the points whose chemical compositions are shown in Table 5. The blue points represent the PdA glass. The red points are CX parts. **d** CaO content (wt.%) of PdA glass close to the carbonate xenoliths (see the text for more details); the various symbols represent the different analyzed transects. The vertical line divides the analysis points carried out on the glass in contact with the carbonate xenolith (Ca-rich glass) and away from it (Ca-normal glass)

Decarbonation of the CXs

Once entrained into the magmatic mixture, the limestone CXs physically and chemically interact with the host magma for the duration of magma ascent up to the fragmentation level, after which the fragmented pumices experience rapid ejection and cooling, terminating any possible further interaction. The timescale of magma ascent from magma chamber to Earth's surface (and hence the upper limit of possible interaction duration of syn-eruptively entrained CXs with ascending magma) is in the range of minutes to tens of minutes for sustained explosive eruptions (e.g., Humphreys et al. 2008; Castro and Dingwell 2009; Costa et al. 2009; Lloyd et al. 2014; Moussallam et al. 2019).

In the following, we discuss the combined effects of decarbonation and diffusive dissolution in terms of heating and volatile release, textural observations, chemical (i.e., diffusive) effects, and, finally, their combined effect on eruption dynamics.

Heating of clasts and volatile release

The effect of heating of carbonate, and the relative reactions, have been described by many authors with respect to industrial applications in the ceramic industry and materials science (e.g., Gunasekaran and Anbalagan 2007; Marinoni et al. 2012; Olszak-Humienik and Jablonski 2015). It should be noted that in these industrial applications, pressures and P_{CO2} conditions are significantly different from natural

Table 4 Major element composition of the patina of carbonate xenoliths, obtained by EDS spectrometer and given in wt.%. The letters and numbers refer to the patinas and spots of chemical analyses shown in Fig. 6

		Na2O	MgO	Al2O3	SiO2	P2O5	SO3	K2O	CaO	TiO2	MnO	FeO	SrO	F	Cl
a AV4	1	-	1.16	-	1.42	-	-	-	97.42	-	-	-	-	-	-
	2	-	-	-	-	-	1.36	-	98.64	-	-	-	-	-	-
	3	-	0.64	-	-	-	-	-	99.36	-	-	-	-	-	-
b AV17-4(1)	1	-	0.55	-	-	-	-	-	99.45	-	-	-	-	-	-
	2	-	1.39	-	0.65	-	0.43	-	97.24	-	-	-	-	-	-
	3	-	1.06	-	0.40	-	0.49	-	97.71	-	-	-	-	-	-
	4	-	0.58	-	-	-	-	-	99.42	-	-	-	-	-	-
c AV3	1	0.24	-	-	-	-	0.48	0.18	96.92	-	-	-	1.04	-	1.15
	2	-	22.35	13.56	59.74	-	-	0.36	4.00	-	-	-	-	-	-
	3	-	2.35	0.88	3.27	-	-	-	92.57	-	-	-	-	-	-
	4	-	1.73	0.66	2.12	-	-	-	94.80	-	-	-	-	-	-
	5	-	0.21	-	0.35	-	0.29	-	94.96	-	-	-	4.18	-	-
	6	0.43	-	-	-	-	1.21	0.24	95.76	-	-	-	1.80	-	0.55
d AV17-1(3)	1	-	0.26	0.54	2.22	-	2.18	-	92.42	-	-	-	-	2.17	0.22
	2	-	0.89	18.23	68.69	-	-	-	6.61	-	-	2.02	-	-	0.66
	3	-	0.29	1.30	4.31	-	0.56	-	92.62	-	-	-	-	0.73	0.20
	4	-	0.29		2.66	-	4.08	-	91.68	-	-	-	-	1.29	-
	5	5.31	0.45	21.25	56.43	-	-	7.87	4.56	0.32	-	3.14	-	-	0.66
	6	-	-	-	-	-	1.81	-	98.19	-	-	-	-	-	-
e AV2	1	-	10.91	2.5	16.67	0.32	-	0.19	43.99	-	-	0.27	-	24.51	0.21
	2	0.21	24.78	7.86	49.84	-	0.54	0.69	11.28	0.35	-	1.04	-	3.15	0.26
	3	0.19	3.83	3.13	14.03	0.24	0.93	0.35	75.01	-	-	0.47	-	0.51	1.31
	4	0.35	0.22	-	-	-	0.53	0.11	96.55	-	-	-	1.24	0.99	-
	5	0.24	0.25	-	-	-	0.49	0.18	96.14	-	-	-	1.78	0.81	0.11
f AV5	1	0.42	0.56	-	-	-	0.42	-	97.46	-	-	-	0.76	0.55	-
	2	0.36	0.55	-	-	-	-	-	96.66	-	-	-	1.68	0.55	0.19
	3	0.42	20.7	12.01	59.15	-	-	0.83	3.84	-	-	1.59	-	1.09	0.26
	4	-	25.12	12.59	52.22	-	0.53	0.24	5.59	-	-	1.49	-	1.61	0.42
	5	-	1.94	-	-	-	1.55	-	96.51	-	-	-	-	-	-

systems. However, here, we use those reactions, at atmospheric pressure, and assume low to absent confining P_{CO2} considering the limestone of CXs is analogous to ceramic materials:

$$CaMg(CO_3)_2 \rightarrow CaCO_3 + MgO + CO_2 \text{ above } 588.K\ (= 315.45°C) \quad (1)$$

$$CaMg(CO_3)_2 \rightarrow MgO + CaO + 2CO_2 \text{ above } 811.3\ K\ (= 538.15°C) \quad (2)$$

$$CaCO_3 \rightarrow CaO + CO_2 \text{ above } 1118.9\ K\ (= 845.75°C) \quad (3)$$

Since the magma temperature was estimated at 850 °C for the tephri-phonolitic (EU3) magma (Pappalardo and Mastrolorenzo 2010), all three reactions can theoretically have been experienced by the CXs entrained during the EU3 phase. It needs to be considered, though, that heating of the entrained CXs is not instantaneous (especially in the CX core) and that depending on entrapment depth, some of the entrained CXs might not have experienced (all of) the reactions mentioned above completely (rim vs. core). Sottili et al. (2010) and Buono et al. (2020) show that heat transfer from magma to the entrained CXs, hence heating the CXs, depends mainly on initial wall-rock temperature and clast size. In their models, centimeter-sized clasts generally reach thermal equilibrium at magmatic temperatures throughout the whole clast within seconds to minutes, while larger clasts require much longer times (i.e., 1–1.5 h for a 10-cm-sized clast, Buono et al. (2020)) and hence might exhibit an unaffected core.

Recent experimental studies have shown that the release of CO_2 from limestones can be a syn-eruptive process at both atmospheric pressure and 0.5 GPa and might be completed within minutes for centimeter-sized clasts (Deegan et al. 2010; Jolis et al. 2013; Knuever et al. 2023). During experiments, the released CO_2 formed gas bubbles, which nucleated around the carbonate clast leading to larger

Table 5 Major element composition of the carbonate xenoliths and glass, obtained by EDS spectrometer and given in wt.%. The letters a, b, and c refer to the picture shown in Fig. 7 and numbers refer to the spots of chemical analysis

		Na2O	MgO	Al2O3	SiO2	P2O5	SO3	K2O	CaO	TiO2	MnO	FeO	SrO	BaO	F	Cl
a	1	4.93	0.57	20.33	55.74	-	-	10.89	2.71	0.60	-	3.76	-	-	-	0.47
	2	5.10	0.51	20.62	55.79	0.16	-	10.81	2.94	0.44	-	3.00	-	-	-	0.61
	3	6.05	0.41	20.25	54.47	-	0.16	11.43	3.94	0.31	-	2.50	-	-	-	0.48
	4	4.96	0.48	19.87	54.02	0.26	0.17	10.37	6.84	0.34	-	2.23	-	-	-	0.48
	5	5.01	0.26	21.96	57.24	-	-	7.50	5.55	0.27	-	1.46	-	0.48	-	0.25
	6	3.13	1.92	18.89	56.64	0.23	-	7.60	9.16	0.29	-	1.32	-	-	0.27	0.56
	7	0.46	0.67	4.01	3.01	-	0.53	0.45	89.42	-	-	0.93	-	-	0.50	-
b	1	6.69	0.30	21.07	56.51	-	-	8.8	3.34	0.21	-	2.42	-	-	-	0.66
	2	6.38	0.32	21.23	56.32	0.19	-	7.75	4.22	0.00	0.22	2.49	-	-	0.29	0.60
	3	7.04	0.22	21.17	56.5	-	-	8.55	3.24	0.24	-	2.42	-	-	0.00	0.62
	4	5.85	0.26	21.24	56.43	-	-	8.04	4.57	0.30	-	2.37	-	-	0.31	0.63
	5	6.52	0.19	22.22	56.39	-	-	8.77	3.1	0.23	-	2.05	-	-	0.00	0.53
	6	5.16	0.33	21.01	56.06	-	-	8.46	5.46	-	-	2.66	-	-	0.27	0.59
	7	4.94	0.32	21.04	55.79	0.17	-	8.64	5.78	-	-	2.49	-	-	0.27	0.57
	8	5.08	0.37	20.70	55.45	0.18	-	7.92	6.70	0.37	-	2.37	-	-	0.29	0.58
	9	5.31	0.25	20.67	55.54	-	-	8.36	6.90	0.27	-	2.18	-	-	-	0.53
	10	1.75	10.7	11.99	64.91	-	0.46	6.08	2.84	-	-	0.47	-	-	0.38	0.44
	11	0.30	0.28	0.30	2.99	-	2.62	0.28	92.61	-	-	-	-	-	0.63	-
c	1	7.53	0.52	20.2	55.26	0.17	0.14	6.65	4.31	0.41	0.15	3.64	-	0.23	-	0.78
	2	6.63	0.57	19.62	54.23	-	-	5.65	8.51	0.51	0.13	3.37	-	-	-	0.78
	3	-	15.36	11.27	49.26	-	0.24	1.38	19.14	0.34	-	2.26	-	-	0.53	0.22
	4	-	-	-	-	-	0.24	0.17	97.26	-	-	-	1.40	-	0.92	-
	5	-	10.12	12.11	56.68	-	-	2.24	13.30	0.59	-	4.47	-	-	0.37	0.11
	6	-	0.21	-	-	-	0.31	0.10	96.94	-	-	-	1.52	-	0.83	0.10
	7	-	3.78	2.00	8.71	-	0.36	0.24	79.13	-	-	0.59	-	-	5.07	0.12
	8	-	3.08	2.02	6.46	-	0.21	0.15	85.33	-	-	0.50	-	-	2.04	0.20
	9	-	0.81	0.29	0.57	-	0.25	-	97.92	-	-	0.17	-	-	-	-
	10	-	1.34	0.24	0.51	-	0.35	-	97.57	-	-	-	-	-	-	-

bubbles grown by coalescence and diffusion (Blythe et al. 2015; Knuever et al. 2023). In the case of the PdA eruption, the CXs were entrapped into the magma between 6 and − 2 km depth, based on volcanological and subsurface stratigraphic data (Sulpizio et al. 2010). At these pressures, the CO_2 solubility in silicate melts is very low or close to zero (Lowenstern 2001; Botcharnikov et al. 2005; Vetere et al. 2014), and the CO_2 released during the syn-eruptive decarbonation must exsolve as a vapor phase. This agrees with the broader vesicle size distribution and the larger vesicle-size values shown by the EU3 top pumice fragments with respect to EU2 and EU3 bottom layers (Figs. 1c and d and 8, and Sulpizio et al. 2010). As observed in Fig. 8, the vesicle size distributions of the juvenile fragment from EU2 and EU3 bottom layers show a similar trend, with the mode of the smaller vesicle subpopulations at 5.75 ϕ, which can be assumed as the last nucleation event, and the coarse tail that can reflect the expansion and coalescence of earlier formed vesicles (Blower et al. 2002; Gonnermann and Houghton 2012; Rotella et al. 2014).

Instead, the broader vesicle-size distribution of the pumices at the top of EU3 (Fig. 8), their larger bubbles hosting remnants of the entrained carbonate clasts (Figs. 2 and 10) with empty spaces around the limestone fragments, and their vesicles with pipe-like structures (Fig. 10) can be related to vesiculation due to the fast release of CO_2 during the decarbonation process suffered by the limestone in contact with the hot melt (Blythe et al. 2015; Knuever et al. 2023).

Similar observations were made in juvenile fragments of the Pomici di Base Plinian eruption of Somma-Vesuvius (Pappalardo et al. 2018). Even though the CXs were not directly observed in the products of that eruption, high vesicle-number densities and multiple cumulative vesicle-size distribution patterns were explained by rapid vesiculation pulses driven by syn-eruptive limestone assimilation during magma ascent through the carbonate bedrock (Pappalardo et al. 2018).

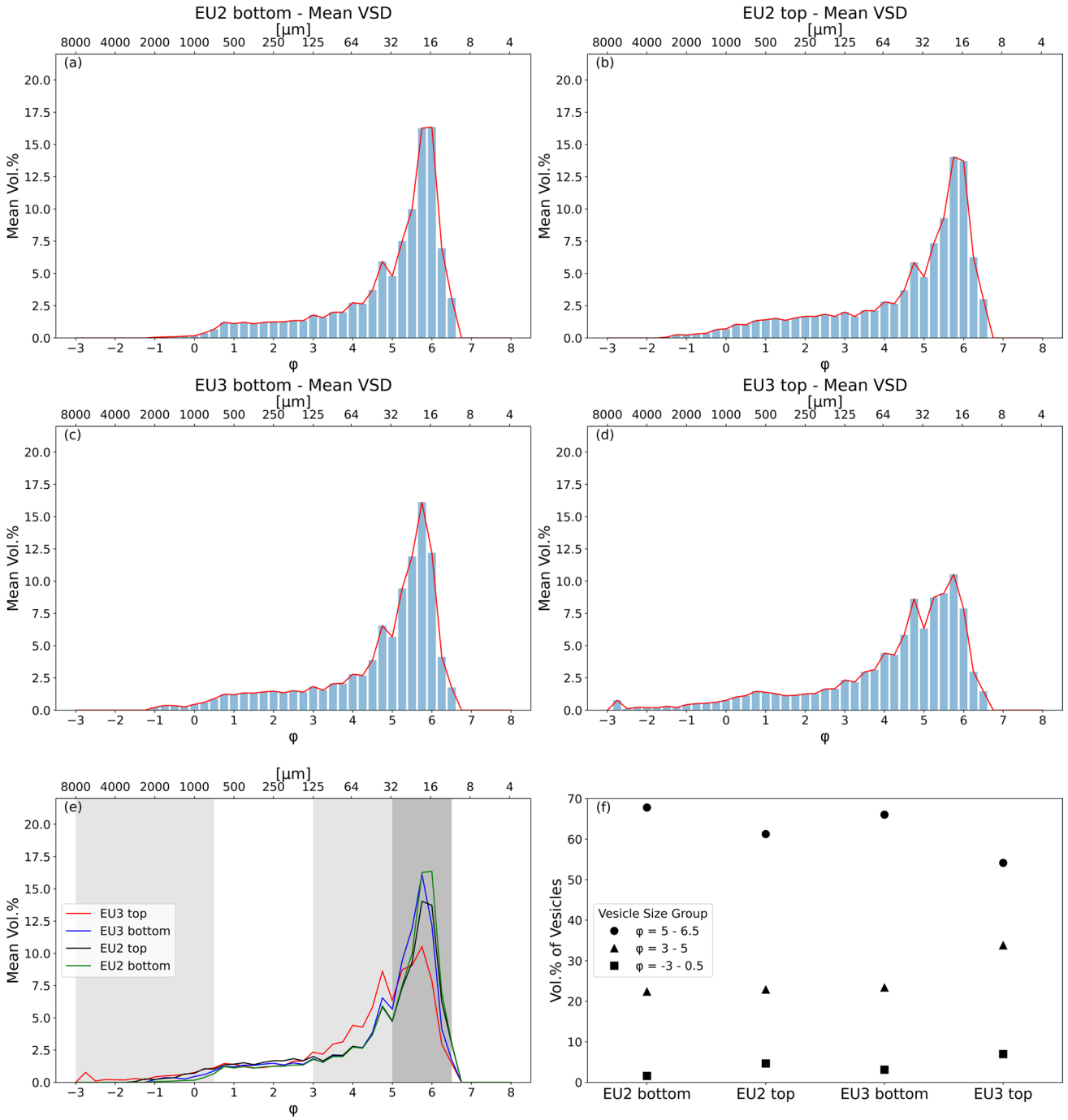

Fig. 8 Vesicle size distribution (VSD) histograms of juvenile fragments from the Plinian phase of the PdA-eruption. **a**–**d** The mean VSD for top and bottom of the two Plinian eruptive units (EU2 and EU3). **e** A comparison of the outlines of the histograms of the four VSDs. **f** The evolution of the volumes (in percent) of the three highlighted vesicle size groups (**e**) throughout the magmatic Plinian phase of the PdA-eruption

Textural observations

Texturally, the CXs are characterized by two to three zones from the border to the core: (1) an outer amorphous rim (Figs. 3, 4, 5), the patina; (2) an internal texturally different zone, the corona; observed only in the white CXs; and (3) a core that still shows the original limestone texture. The patina is characterized by the loss of the original limestone texture, an increase in porosity, cracks, and voids, as well as the development of a dendritic texture on the border of the CXs (Figs. 3, 4, 5, and 6).

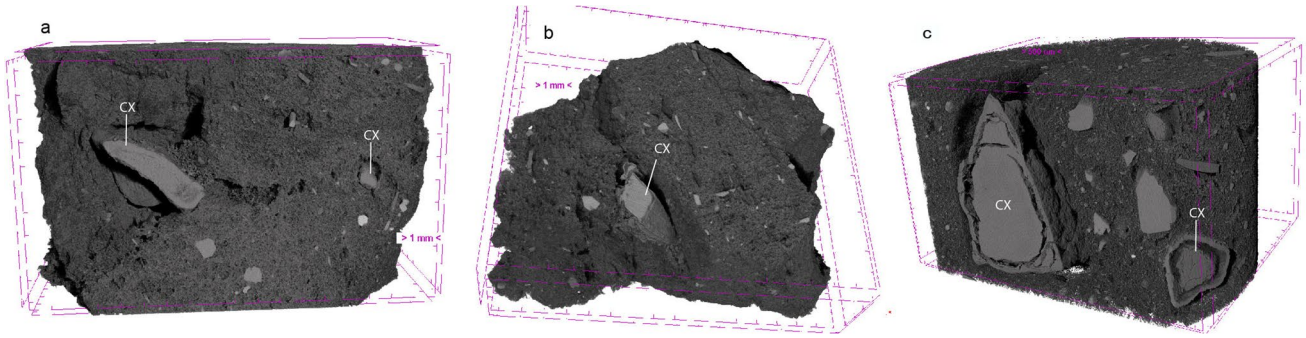

Fig. 9 3D volume rendering images of three pumices with carbonate xenoliths (CX)

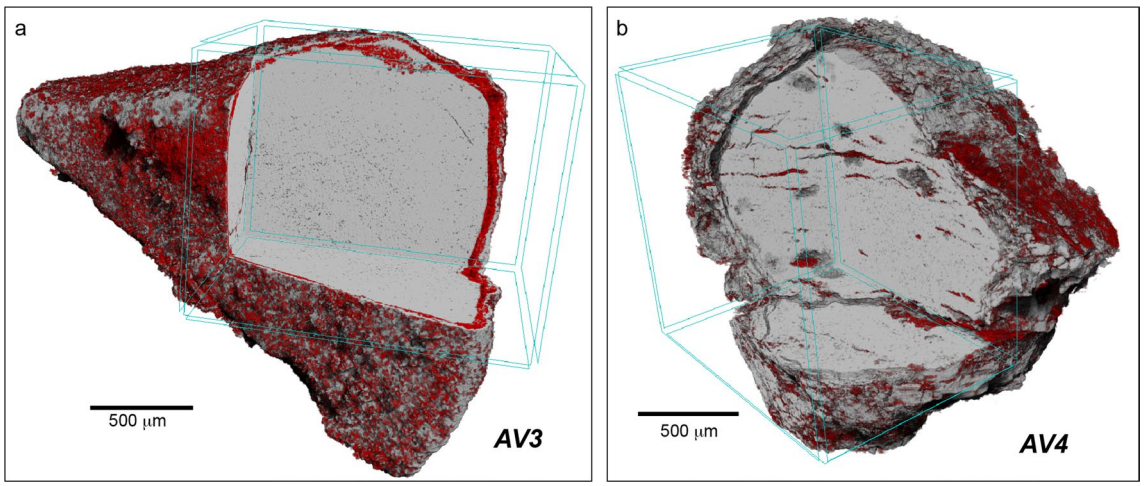

Fig. 10 3D volume rendering images of two carbonate xenoliths (CX). **a** White CX, **b** (dark-)grey CX. In red color, material with a low attenuation coefficient value. In grey color, the material with a high attenuation coefficient value (i.e., CaO-rich materials). See the text for more details. Sky blue box represents the cutting shape of fragments

Several studies on quicklime production (Fuertes et al. 1993; Ghiasi et al. 2021) and ceramic firing experiments (Cultrone et al. 2001; Tschegg et al. 2009; Allegretta et al. 2016) have shown that the decomposition of carbonate fragments occurs in a well-defined border, called "reaction front." In their heating experiments, Zhang et al. (2017) observed the development of cracks and voids in the carbonate fragments starting from 300 to 800 °C, respectively. The reaction front progresses continuously towards the particle core as the reaction proceeds (Ingraham and Marier 1963; Ghiasi et al. 2021). Furthermore, Baker (1962) and Peretyazhko et al. (2021) demonstrated how, at high temperatures ($T > 1240$ °C) and low pressures ($P > 4$ MPa) entrained limestone clasts do not decompose thermally but form an amorphous solid phase, which may decarbonize and dissolve via diffusion and surface reaction. Although the behavior at lower temperatures (and low pressures) is not entirely clear, short-term contact metamorphism during magma ascent might be a possible explanation for the amorphous rims found in the CXs (Figs. 5, 6, and 7).

The presence of a core that still shows the original limestone texture suggests that the coarser CXs did not suffer a complete decarbonation process (Figs. 5 and 6). However, this cannot be excluded for the clasts smaller than 2 mm, where a large space between the patina and the inner part of the limestone was observed, as well as abundant fractures in the core (Fig. 9c).

The occasional presence of well-defined scalenohedral calcite crystals at the border of the CX patinas, which sometimes form a rosette texture on the patina surface, suggests that a secondary recrystallization process might have occurred after the emplacement of the pyroclastic deposit. As an example, these crystal shapes were observed during the transformation of portlandite ($Ca(OH)_2$) to calcite in industrial experiments (García-Carmona et al. 2003; Galan et al. 2015; Jimoh et al. 2017; Silva et al. 2021). We assume that, due to the high open vesicularity of juvenile deposits,

circulating fluids reacted with the residual carbonate outer zones, forming calcite crystals.

Clast dissolution and diffusion

While it is likely that some of the smaller CXs were completely dissolved, the presence of bigger CXs within the pumice suggests that the dissolution process of entrained limestone was not complete. The increase of CaO over a thickness of only a few microns in the glass in direct contact with CXs (Fig. 7 and Table 5) suggests that the chemical dissolution via diffusion or surface reaction, while present, was not extensive. This evidence agrees with the results of Knuever et al. (2023) who observed an incomplete dissolution of the entrained limestone clasts in their experiments with phonolitic melts (EU3 pumice of PdA) at atmospheric pressure (with an experimental duration of up to 30 min). In particular, the 950 °C set of experiments of Knuever et al. (2023), where diffusion of Ca into an anhydrous phonolitic melt was restricted to only several tens of microns, agrees with the observations made here in natural samples. Furthermore, Knuever et al. (2023) suggested that the absence of prolonged direct contact, caused by bubble formation around the limestone clast after entrapment, was a factor in restricting the complete dissolution via diffusion or surface reaction. This also agrees with the observation made here where the CXs are surrounded by large bubbles (Figs. 2 and 9).

On the other hand, when pressure is above atmospheric (> 1 atm), which is likely in our case since limestone clasts entrainment occurred at a depth between 2 and 6 km, dissolution is faster, as demonstrated by experiments at 0.5 GPa (Deegan et al. 2010; Jolis et al. 2013; Blythe et al. 2015). In these experimental works, the entrained limestone clasts were completely dissolved within minutes. However, pressure and temperature conditions (0.5 GPa and 1200 °C), as well as melt composition (hydrous (~2 wt.%) and anhydrous basaltic andesite and hydrous (~2 wt.%) shoshonite), do not meet the conditions of the PdA eruption. Even for a lower pressure (i.e., 0.15 GPa), which is plausible during the final magma ascent of the EU3-phase of the PdA eruption, Deegan et al. (2023) demonstrated complete dissolution of carbonate compounds within minutes in anhydrous and slightly hydrated (0.5 wt.%) magma-shale interaction experiments. To match and compare evidence, further experimental investigations with systematic variations of pressure, temperature, and melt composition are needed.

However, the presence of Na, Si, K, Al, and Fe inside the CX patinas and in the areas between the vesiculated glass of PdA pumices and the CXs (Figs. 6 and 7; Tables 4 and 5) suggests that mass transport of melt constituents must have occurred. The precise dynamics of how melt constituents may have diffused (e.g., via crack/pore filling) is beyond the scope of this paper and asks for further investigation. Some hints come from ceramic firing experiments (Cultrone et al. 2001; Tschegg et al. 2009), where the transformation of $CaCO_3$ or $CaMg(CO_3)_2$ into their components CaO, MgO, and CO_2 creates space (pores, cracks), where melt constituents may have had room to generate a second-stage reaction domain.

Further evidence for a low-grade diffusion process comes from the white CXs, where the EDS transects show an Mg enrichment in the corona (Fig. 3d–f). The same behavior was observed on Mg-calcite fragments during ceramic firing experiments with a temperature range of 850–1000 °C (Cultrone et al. 2001) and, recently, in short-term magma-carbonate interaction experiments at atmospheric pressure (Knuever et al. 2023). Cultrone et al. (2001) suggest that during the decarbonation processes, Ca is preferentially leached out of the former Mg-calcite clast. This is because the mobility of Ca^{2+} is greater than that of Mg^{2+} due to small differences in ion size and electronegativity (Allen et al. 2009; Yoon et al. 2023). It follows that Ca^{2+} can leave the carbonate and react to the surrounding environment to form Ca-silicate compounds when in contact with ambient air at low temperatures (Yoon et al. 2023). In some cases (Fig. 3a–c), the outer part of the corona shows a very high concentration of Ca, which reflects the redeposition of Ca leached out from the inner part of the corona. The third type of clasts in Fig. 3g–i shows pervasive leaching of Ca to the outer part of the corona. The clasts of this category may represent a complete leaching of Ca, with enhanced separation of Ca and Mg within the clast. The three different types of leaching probably reflect different thermo-metamorphism reactions due to different contact times between the CX and the magma.

Effects on eruptive dynamics

Gas exsolution with bubble formation inside magma is one of the main driving mechanisms for the sustainment of the mass-flow rate of explosive eruptions (e.g., Ida 2007; Pyle 2015). Undoubtedly, the thermo-metamorphic reactions producing CO_2 have supplied extra volatiles to the melt of the final phase of EU3, but it is hard to establish to what extent. It is clear that the gas content did not decline, as should have been expected in an eruption that in the final phase was fed by a less evolved magma with respect to that of the preceding phase (tephritic/phonolitic vs phonolitic/tephritic). This is suggested by the higher vesicularity of the EU3 top pumice fragments (average 71%) compared to that of EU2 top (around 65%; Fig. 1c) or EU3 base (around 68%; Fig. 1c). This means that an additional contribution from decarbonation would have helped the increase of vesicularity and buoyancy of the EU3 top magma, favoring magma ascent rate and eruption sustainment. Based on average vesicularity data, the contribution to gas content of decarbonation

process is around 0.5×10^6 m^3 or 0.2×10^6 m^3 considering as reference the average vesicularity of EU2 top or EU3 base, respectively. If we consider the maximum variability in vesicularity of the EU2 top and EU3 base with respect to the EU3 top, we obtained a contribution of 1.2×10^6 m^3 or 0.9×10^6 m^3.

From the assessment of Hanson (2016), we know that the amount of carbonates within juvenile clasts of the EU3 top layer is in the order of 5×10^7 kg. Because CO_2 accounts for around 43% of carbonate weight, if we assume a total breakdown of carbonates, we obtain around 2×10^7 kg (or 10^7 m^3) of volatiles released into the magma. This simple calculation indicates incomplete decarbonation of entrapped CXs during the final part of the magmatic phase of PdA eruption.

Experimental data to compare these theoretical calculations are scarce. The closest data in terms of melt composition, temperature, and pressure conditions are decarbonation curves of Knuever et al. (2023) at 950 °C, atmospheric pressure, and within a phonolite melt. After Knuever et al. (2023), a releasing time between 30 and 60 s is expected if a 3 to 6% increase in vesicularity is to be attributed to decarbonation. Even considering the maximum values of 13% and 17%, the decarbonation time ranges between 130 and 170 s. While the melt composition, temperature, and pressure condition of the natural case are different, the experimental data help to give us an idea about CO_2 release time. Furthermore, these time ranges are reasonable values, when compared to theoretically calculated magma ascent times for sustained explosive Plinian eruptions, which are in the order of several minutes (e.g., Costa et al. 2009).

Conclusions

Macroscopic, microscopic, and microtomographic textural observations, as well as geochemical investigation of limestone clasts inside juvenile pumices, indicate that a short-term carbonate assimilation process occurred during the EU3 final phase of the PdA eruption. The timescale of decarbonation process, as evidenced by experiments of magma-carbonate interaction, carried out at both atmospheric and 0.5–1.0 GPa pressures (Deegan et al. 2010; Jolis et al. 2013; Blythe et al. 2015; Knuever et al. 2023), fits with the transit time of magma within the feeding dike during a sustained explosive eruption, which was estimated in the order of minutes to tens of minutes (Humphreys et al. 2008; Castro and Dingwell 2009; Costa et al. 2009; Lloyd et al. 2014; Moussallam et al. 2019).

The addition of new gas bubbles, related to the release of CO_2, likely increased the buoyancy and driving pressure (Gudmundsson 2012) of the magmatic mixture, leading to a larger mass-eruption rate (La Spina et al. 2022). Moreover, the recent numerical modeling of the PdA plumbing system suggested that the increase in CXs, originating from the feeding dike walls in the EU3 phase, was the result of the elastic response of the feeding dike (i.e., decrease in its diameter) and the progressive exhaustion of the magmatic driving pressure (Massaro et al. 2018). In this regard, our results show that the decarbonation helped to sustain the eruption rate by slightly increasing the vesicularity (< 10%) of the magma. Our results differ from the mechanism of magma-carbonate interaction suggested by Buono et al. (2020) for the Pomici di Base eruption of Somma-Vesuvius, but they contribute to the understanding of the "anomalous" explosivity of Plinian eruptions fed by magmas erupting through to carbonate country rocks.

Acknowledgements The authors thank Rebecca Morris and an anonymous reviewer, as well as associate editor Pierre-Simon Ross, for their constructive suggestions that helped to improve the manuscript. The authors also thank Francesco Campanale for the preparation of the thin sections and Nicola Mongelli for his professional technical assistance during the SEM measurements.

Funding Open access funding provided by Università degli Studi di Bari Aldo Moro within the CRUI-CARE Agreement. The Bruker Skyscan 1172 high-resolution μX-CT scanner has been purchased with funds from "PON Ricerca e Competività 2007–2013". This study was carried out within the RETURN Extended Partnership and received funding from the European Union Next-Generation NGEU (National Recovery and Resilience Plan – NRRP, Mission 4, Component 2, Investment 1.3 – D.D. 1243 2/8/2022, PE0000005). SM was also supported by the PON Research and Innovation 2014–2020 project referring to research contracts on green topics (grant no. CODICE CUP H95F21001440006).

Open Access This article is licensed under a Creative Commons Attribution 4.0 International License, which permits use, sharing, adaptation, distribution and reproduction in any medium or format, as long as you give appropriate credit to the original author(s) and the source, provide a link to the Creative Commons licence, and indicate if changes were made. The images or other third party material in this article are included in the article's Creative Commons licence, unless indicated otherwise in a credit line to the material. If material is not included in the article's Creative Commons licence and your intended use is not permitted by statutory regulation or exceeds the permitted use, you will need to obtain permission directly from the copyright holder. To view a copy of this licence, visit http://creativecommons.org/licenses/by/4.0/.

References

Allegretta I, Pinto D, Eramo G (2016) Effects of grain size on the reactivity of limestone temper in a kaolinitic clay. Appl Clay Sci 126:223–234. https://doi.org/10.1016/J.CLAY.2016.03.020

Allen JP, Parker SC, Price DW (2009) Atomistic simulation of the surface carbonation of calcium and magnesium oxide surfaces. J Phys Chem C 113(19):8320–8328. https://doi.org/10.1021/jp810885m

Baker E (1962) The calcium oxide–carbon dioxide system in the pressure range 1–300 atmospheres. J Chem Soc (Resumed) 0:464–470

Blower JD, Keating JP, Mader HM, Phillips JC (2002) The evolution of bubble size distributions in volcanic eruptions. J Volcanol Geotherm Res 120:1–23

Blythe LS, Deegan FM, Freda C, Jolis EM, Masotta M, Misiti V, Taddeucci J, Troll VR (2015) CO2 bubble generation and migration

during magma–carbonate interaction. Contrib Mineral Petrol 169:1–16. https://doi.org/10.1007/s00410-015-1137-4
Borisova AY, Bohrson WA (2023) How is carbonate crust digested by magma? Front Earth Sci 11:1186207
Borisova AY, Martel C, Gouy S, Pratomo I, Sumarti S, Toutain JP, Bindeman IN, de Parseval P, Metaxian JP (2013) Highly explosive 2010 Merapi eruption: evidence for shallow-level crustal assimilation and hybrid fluid. J Volcanol Geoth Res 261:193–208. https://doi.org/10.1016/j.jvolgeores.2012.11.002
Botcharnikov R, Freise M, Holtz F, Behrens H (2005) Solubility of C-O-H mixtures in natural melts: new experimental data and application range of recent models. Ann Geophys 48:633–646
Buono G, Pappalardo L, Harris C, Edwards BR, Petrosino P (2020) Magmatic stoping during the caldera-forming Pomici di Base eruption (Somma–Vesuvius, Italy) as a fuel of eruption explosivity. Lithos 370–371:105628. https://doi.org/10.1016/j.lithos.2020.105628
Caggiani MR, Ditaranto N, Guascito MR, Acquafredda P, Laviano R, Giannossa LC, Mutino S, Mangone A (2015) Combined analysis of enameled and gilded glassware from Frederick II Castle at Melfi (Italy) to identify technology and raw materials. X-Ray Spectrom 44:191–200
Caricchi L, Sheldrake TE, Blundy J (2018) Modulation of magmatic processes by CO_2 flushing. Earth Planet Sci Lett 491:160–171. https://doi.org/10.1016/j.epsl.2018.03.042
Caricchi L, Montagna CP, Aiuppa A, Lages J, Tamburello G, Papale P (2024) CO_2 flushing triggers paroxysmal eruptions at open conduit basaltic volcanoes. J Geophys Res 129. https://doi.org/10.1029/2023JB028486
Castro JM, Dingwell DB (2009) Rapid ascent of rhyolitic magma at Chaitén Volcano, Chile. Nature 461:780–783. https://doi.org/10.1038/nature08458
Chadwick JP, Troll VR, Ginibre C, Morgan D, Gertisser R, Waight TE, Davidson JP (2007) Carbonate assimilation at Merapi volcano, Java, Indonesia: insights from crystal isotope stratigraphy. J Petrol 48:1793–1812
Costa A, Sparks RSJ, Macedonio G, Melnik O (2009) Effects of wall rock elasticity on magma flow in dykes during explosive eruptions. Earth Planet Sci Lett 288:455–462
Cross JK, Tomlinson EL, Giordano G, Smith VC, De Benedetti AA, Roberge J, Manning CJ, Wulf S, Menzies MA (2014) High level triggers for explosive mafic volcanism: Albano Maar, Italy. Lithos 190–191:137–153. https://doi.org/10.1016/j.lithos.2013.11.001
Cultrone G, Rodriguez-Navarro C, Sebastian E, Cazalla O, De la Torre MJ (2001) Carbonate and silicate phase reactions during ceramic firing. Eur J Mineral 13:621–634
Dallai L, Cioni R, Boschi C, D'Oriano C (2011) Carbonate-derived CO_2 purging magma at depth: influence on the eruptive activity of Somma-Vesuvius, Italy. Earth Planet Sci Lett 310:84–95
Deegan FM, Troll VR, Freda C, Misiti V, Chadwick JP, McLeod CL, Davidson JP (2010) Magma-carbonate interaction processes and associated CO_2 release at Merapi volcano, Indonesia: insights from experimental petrology. J Petrol 51:1027–1051
Deegan FM, Troll VR, Freda C, Misiti V, Chadwick JP (2011) Fast and furious: crustal CO_2 release at Merapi volcano, Indonesia. Geol Today 27:57–58
Deegan FM, Troll VR, Gertisser R, Freda C (2023) Magma-carbonate interaction at Merapi Volcano, Indonesia. In: Gertisser R, Troll VR, Walter TR, Nandaka IGMA, Ratdomopurbo A (eds) Merapi Volcano. Active volcanoes of the world. Springer. https://doi.org/10.1007/978-3-031-15040-1_10
del Moro A, Fulignati P, Marianelli P, Sbrana A (2001) Magma contamination by direct wall rock interaction: constraints from xenoliths from the walls of a carbonate-hosted magma chamber (Vesuvius 1944 eruption). J Volcanol Geoth Res 112:15–24
Dioguardi F, Dellino P (2014) PYFLOW: a computer code for the calculation of the impact parameters of dilute pyroclastic density current (DPDC) based on field data. Comput Geosci 66:200–210. https://doi.org/10.1016/j.cageo.2014.01.013
dos Reis PJ, Nagata R, Appoloni CR (2017) Pore size distributions convolution for microtomographic images applied to Shark Bay's oolite. Micron 98:49–54
Feldkamp LA, Davis LC, Kress JW (1984) Practical conebeam algorithm. J Opt Soc Am A 1:612–619
Freda C, Gaeta M, Palladino DM, Trigila R (1997) The Villa Senni Eruption (Alban Hills, Central Italy): the role of H_2O and CO_2 on the magma chamber evolution and on the eruptive scenario. J Volcanol Geoth Res 78:103–120
Freda C, Gaeta M, Giaccio B, Marra F, Palladino DM, Scarlato P, Sottili G (2011) CO_2-driven large mafic explosive eruptions: the Pozzolane Rosse case study from the Colli Albani Volcanic District (Italy). Bull Volcanol 73:241–256. https://doi.org/10.1007/s00445-010-0406-3
Fuertes A, Marban G, Rubiera F (1993) Kinetics of thermal decomposition of limestone particles in a fluidized bed reactor. Chem Eng Res Des 71:421–428
Fulignati P, Marianelli P, Santacroce R, Sbrana A (2004) Probing the Vesuvius magma chamber–host rock interface through xenoliths. Geol Mag 141:417–428
Galan I, Glasser FP, Baza D, Andrade C (2015) Assessment of the protective effect of carbonation on portlandite crystals. Cem Concr Res 74:68–77
García-Carmona J, Gómez-Morales J, Rodríguez-Clemente R (2003) Morphological control of precipitated calcite obtained by adjusting the electrical conductivity in the $Ca(OH)_2$–H_2O-CO_2 system. J Cryst Growth 249:561–571
Ghiasi M, Abdollahy M, Khalesi M (2021) Investigating the kinetics, mechanism, and activation energy of limestone calcination using isothermal analysis methods. Min Metall Explor 38:129–140. https://doi.org/10.1007/s42461-020-00300-y
Gilg HA, Lima A, Somma R, Belkin HE, De Vivo B, Ayuso RA (2001) Isotope geochemistry and fluid inclusions study of skarns from Vesuvius. Mineral Petrol 73:145–176
Giuffrida M, Holtz F, Vetere F, Viccaro M (2017) Effects of CO_2 flushing on crystal textures and compositions: experimental evidence from recent K-trachybasalts erupted at Mt. Etna. Contrib Mineral Petrol 172:90. https://doi.org/10.1007/s00410-017-1408-3
Goff F, Love SP, Warren RG, Counce D, Obenholzner J, Siebe C, Schmidt SC (2001) Passive infrared remote sensing evidence for large, intermittent CO emissions at Popocatepetl volcano, Mexicó. Chem Geol 177:133–156
Gonnermann HM, Houghton BF (2012) Magma degassing during the Plinian eruption of Novarupta, Alaska, 1912. Geochem Geophys Geosyst 13(10):Q10009
Gudmundsson A (2012) Magma chambers: formation, local stresses, excess pressures, and compartments. J Volcanol Geoth Res 237–238:19–41. https://doi.org/10.1016/j.jvolgeores.2012.05.015
Gunasekaran S, Anbalagan G (2007) Thermal decomposition of natural dolomite. Bull Mater Sci 30:339–344
Hanson J (2016) Conduit evolution during the Avellino eruption at Vesuvius based on lithic abundance and componentry. PhD Thesis. University of Bristol, Bristol, UK
Humphreys M, Menand T, Blundy JD, Klimm K (2008) Magma ascent rates in explosive eruptions: constraints from H_2O diffusion in melt inclusions. Earth Planet Sci Lett 270:25–40
Iacono-Marziano G, Gaillar F, Pichavant M (2008) Limestone assimilation by basaltic magmas: an experimental re-assessment and application to Italian volcanoes. Contrib Mineral Petrol 155:719–738. https://doi.org/10.1007/s00410-007-0267-8

Iacono-Marziano G, Gaillard F, Scaillet B, Pichavant M, Chiodini G (2009) Role of non-mantle CO_2 in the dynamics of volcano degassing: the Mount Vesuvius example. Geology 37:319–322

Ida Y (2007) Driving force of lateral permeable gas flow in magma and the criterion of explosive and effusive eruptions. J Volcanol Geotherm Res 162(3–4):172–184

Ingraham JR, Marier P (1963) Kinetic studies on the thermal decomposition of calcium carbonate. Can J Chem Eng 41:170–173

Inman DL (1952) Measures of describing the size distribution of sediments. J Sediment Petrol 22:125–145

Jimoh OA, Otitoju TA, Hussin H, Ariffin KS, Baharun N (2017) Understanding the precipitated calcium carbonate (PCC) production mechanism and its characteristics in the liquid-gas system using milk of lime (MOL) suspension. S Afr J chem 70:01–07. https://doi.org/10.17159/0379-4350/2017/v70a1

Jolis EM, Freda C, Troll VR, Deegan FM, Blythe LS, McLeod CL, Davidson JP (2013) Experimental simulation of magma-carbonate interaction beneath Mt. Vesuvius, Italy. Contrib Mineral Petrol 166:1335–1353. https://doi.org/10.1007/s00410-013-0931-0

Jolis EM, Troll VR, Harris C, Freda C, Gaeta M, Orsi G, Siebe C (2015) Skarn xenolith record crustal CO_2 liberation during Pompeii and Pollena eruptions, Vesuvius volcanic system, central Italy. Chem Geol 415:17–36. https://doi.org/10.1016/j.chemgeo.2015.09.003

Knuever M, Sulpizio R, Mele D, Pisello A, Costa A, Perugini D, Vetere F (2023) Decarbonation and clast dissolution timescales for short-term magma-carbonate interactions in the volcanic feeding system and their influence on eruptive dynamics: insights from experiments at atmospheric pressure. Chem Geol 639:121724

Knuever M, Sulpizio R, Mele D, Costa A (2022) Magma–rock interactions: a review of their influence on magma rising processes with emphasis on short-timescale assimilation of carbonate rocks. Geological Society, London, Special Publications SP520–2021–177. https://doi.org/10.1144/sp520-2021-177

La Spina G, Arzilli F, Burton M, Polacci M, Clarke A (2022) Role of volatiles in highly explosive basaltic eruptions. Commun Earth Environ 3:156. https://doi.org/10.1038/s43247-022-00479-6

Lloyd AS, Ruprecht P, Hauri EH, Rose W, Gonnermann HM, Plank T (2014) NanoSIMS results from olivine-hosted melt embayments: magma ascent rate during explosive basaltic eruptions. J Volcanol Geoth Res 283:1–18. https://doi.org/10.1016/j.jvolgeores.2014.06.002

Lowenstern JB (2001) Carbon dioxide in magmas and implications for hydrothermal systems. Miner Depos 36:490–502. https://doi.org/10.1007/s001260100185

Marinoni N, Allevi S, Marchi M, Dapiaggi M (2012) A kinetic study of thermal decomposition of limestone using in situ high temperature X-ray powder diffraction. J Am Ceram Soc 95:2491–2498. https://doi.org/10.1111/j.1551-2916.2012.05207.x

Mason E, Edmonds M, Tuchyn AV (2017) Remobilization of crustal carbon may dominate volcanic arc emissions. Science 357:290–294

Massaro S, Costa A, Sulpizio R (2018) Evolution of the magma feeding system during a Plinian eruption: the case of Pomici di Avellino eruption of Somma-Vesuvius, Italy. Earth Planet Sci Lett 482:545–555

Mollo S, Gaeta M, Freda C, di Rocco T, Misiti V, Scarlato P (2010) Carbonate assimilation in magmas: a reappraisal based on experimental petrology. Lithos 114:503–514. https://doi.org/10.1016/j.lithos.2009.10.013

Moussallam Y, Rose-Koga EF, Koga KT, Médard E, Bani P, Devidal JL, Tari D (2019) Fast ascent rate during the 2017–2018 Plinian eruption of Ambae (Aoba) volcano: a petrological investigation. Contrib Mineral Petrol 174:90. https://doi.org/10.1007/s00410-019-1625-1059z

Nagata R, dos Reis PJ, Appoloni CR (2023) Multi-scale approach to assess total porosity and pore size in four different kinds of carbonate rocks. Micron 164:103385

Olszak-Humienik M, Jablonski M (2015) Thermal behavior of natural dolomite. J Therm Anal Calorim 119:2239–2248. https://doi.org/10.1007/s10973-014-4301-6

Otsu N (1979) A threshold selection method from gray-level histograms. IEEE Trans on Syst Man Cyber 9:62–66. https://doi.org/10.1109/TSMC.1979.4310076

Pappalardo L, Mastrolorenzo G (2010) Short residence times for alkaline Vesuvius magmas in a multi-depth supply system: evidence from geochemical and textural studies. Earth Planet Sci Lett 296:133–143

Pappalardo L, Buono G, Fanara S, Petrosino P (2018) Combining textural and geochemical investigations to explore the dynamics of magma ascent during Plinian eruptions: a Somma-Vesuvius volcano (Italy) case study. Contrib Mineral Petrol 173:61. https://doi.org/10.1007/s00410-018-1486-x

Pappalardo L, Buono G, Fanara S, Yi J, Shan X, Guo Z, Zhang M, Ventura G (2023) The role of CO_2 flushing in triggering the 'Millennium' eruption and recent unrests at Changbaishan volcano (China/North Korea). Int Geol Rev 65(5):706–719. https://doi.org/10.1080/00206814.2022.2065544

Peretyazhko IS, Savina EA, Khromova EA (2021) Low-pressure (>4 MPa) and high temperature (>1250 ◦C) incongruent melting of marly limestone: formation of carbonate melt and melilite–nepheline paralava in the khamaryn–khural–khiid combustion metamorphic complex, East Mongolia. Contrib Mineral Petrol 176:38. https://doi.org/10.1007/s00410-021-01794-5

Pichavant M, Scaillet B, Pommier A, Iacono-Marziano G, Cioni R (2014) Nature and evolution of primitive Vesuvius magmas: an experimental study. J Petrol 55:2281–2310

Pyle DM (2015) Sizes of volcanic eruptions. In: The encyclopedia of volcanoes, second ed. Academic Press, pp 257–264. https://doi.org/10.1016/B978-0-12-385938-9.00063-8

Remy E, Thiel E (2002) Medial axis for chamfer distances: computing look-up tables and neighbourhoods in 2D or 3D. Pattern Recogn Lett 23:649–661

Rosi M, Principe C, Vecci R (1993) The 1631 Vesuvius eruption. A reconstruction based on historical and stratigraphical data. J Volcanol Geotherm Res 58:151–182

Rotella MD, Wilson CJN, Barker SJ, Cashman KV, Houghton BF, Wright IC (2014) Bubble development in explosive silicic eruptions: insights from pyroclast vesicularity textures from Raoul volcano (Kermadec arc). Bull Volcanol 76:826

Santacroce R (1987). Somma-Vesuvius. Quaderni della Ricerca Scientifica 114, 8. CNR, pp 1–251

Schaaf P, Stimac J, Siebe C, Macias JL (2005) Geochemical evidence for mantle origin and crustal processes in volcanic rocks from Popocate´petl and surrounding monogenetic volcanoes, Central Mexico. J Petrol 46:1243–1282

Sevink J, van Bergen M, van der Plicht J, Feiken H, Anastasia C, Hizinga A (2011) Robust date for the Bronze Age Avellino eruption (Somma-Vesuvius): 3945±10 calBP (1995±10 calBC). Qua Sci Rev 30:1035–1046

Silva BA, Ferreira Pinto AP, Gomes A, Candeias A (2021) Effects of natural and accelerated carbonation on the properties of lime-based materials. J CO_2 Util 49:101552

Sottili G, Taddeucci J, Palladino DM, Gaeta M, Scarlato P, Ventura G (2009) Subsurface dynamics and eruptive styles of maars in the Colli Albani Volcanic District, Central Italy. J Volcanol Geotherm Res 180:189–202. https://doi.org/10.1016/j.jvolgeores.2008.07.022

Sottili G, Taddeucci J, Palladino DM (2010) Constraints on magma-wall rock thermal interaction during explosive eruptions from textural analysis of cored bombs. J Volcanol Geotherm Res 192:27–34. https://doi.org/10.1016/j.jvolgeores.2010.02.003

Sulpizio R, Mele D, Dellino P, La Volpe L (2005) A complex, Subplinian-type eruption from low-viscosity, phonolitic to tephri-phonolitic magma: the AD 472 (Pollena) eruption of Somma-Vesuvius, Italy. Bull Volcanol 67:743–767

Sulpizio R, Cioni R, di Vito MA, Mele D, Bonasia R, Dellino P (2010) The Pomici di Avellino eruption of Somma-Vesuvius (3.9 ka bp). Part I: Stratigraphy, compositional variability and eruptive dynamics. Bull Volcanol 72:539–558. https://doi.org/10.1007/s00445-009-0339-x

Troll VR, Hilton DR, Jolis EM, Chadwick JP, Blythe LS, Deegan FM, Schwarzkopf LM, Zimmer M (2012) Crustal CO_2 liberation during the 2006 eruption and earthquake events at Merapi volcano. Indonesia. Geophys Res Lett 39:L11302. https://doi.org/10.1029/2012GL051307

Troll VR, Deegan FM, Jolis EM, Harris C, Chadwick JP, Gertisser R, Schwarzkopf LM, Borisova AY, Bindeman IN, Sumarti S, Preece K (2013) Magmatic differentiation processes at Merapi Volcano: inclusions petrology and oxygen isotopes. J Volcanol Geotherm Res 261:38–49. https://doi.org/10.1016/j.jvolgeores.2012.11001

Tschegg C, Ntaflos T, Hein I (2009) Thermally triggered two-stage reaction of carbonates and clay during ceramic firing – a case study on Bronze Age Cypriot ceramics. Appl Clay Sci 43:69–78

Vetere F, Holtz F, Behrens H, Botcharnikov RE, Fanara S (2014) The effect of alkalis and polymerization on the solubility of H_2O and CO_2 in alkali-rich silicate melts. Contrib Mineral Petrol 167:1014. https://doi.org/10.1007/s00410-014-1014-6

Werner C, Brantley S (2003) CO_2 emissions from the Yellowstone volcanic system. Geochem Geophys Geosyst 4:1061

Yoon H, Yoon T, Lee CJ, Yooh S (2023) Kinetic conversion of magnesium and calcium ions of dolomite into useful value-added products using CO_2. Chem Eng J 469:143684. https://doi.org/10.1016/j.cej.2023.143684

Zhang Y, Sun Q, Geng J (2017) Microstructural characterization of limestone exposed to heat with XRD, SEM and TG-DSC. Mater Charact 134:285–295